Department of Physics and Astronomy
University of Heidelberg

Bachelor Thesis in Physics
submitted by

Paul Marie
born in Levallois-Perret (France)

2017

Optical spectroscopy of highly charged ruthenium ions with astrophysical interest

This Bachelor Thesis has been carried out by Paul Marie at the
Max-Planck Institut für Kernphysik in Heidelberg
under the supervision of
PD Dr. José R. Crespo López-Urrutia

Abstract:

Spectroscopic investigations into the abundances of trans-iron elements in stars yield valuable information about stellar evolution. In order to interpret the emission spectrum of these stars, spectral data of trans-iron elements is required. Ruthenium (Z=44) is particularly interesting as it has a similar atomic structure to that of technetium (Z=43), the lightest unstable element. The half-life of technetium is short compared to the life time of a star, allowing a time dependent insight into stellar evolution. In this work, highly charged ruthenium ions were produced and investigated in the Heidelberg electron beam ion trap at the Max Planck Institute of Nuclear Physics in Heidelberg. The fluorescence light emitted by the excited ions was recorded using a Czerny-Turner monochromator. The 53 measured optical lines of the charge states Ru^{9+} to Ru^{18+} were compared to calculations from atomic theory, leading to tentative identifications of 30 transitions.

Zusammenfassung:

Spektroskopische Untersuchungen der Häufigkeiten von Trans-Eisen Elementen in Sternen erbringen wertvolle Informationen über die Sternentwicklung. Um die Emissionsspektren dieser Sterne zu interpretieren, werden spektrale Daten von Trans-Eisen Elementen benötigt. Ruthenium (Z=44) ist hierbei besonders interessant, da seine atomare Struktur der von Technetium (Z=43) sehr ähnelt. Technetium ist das leichteste Element, welches keine stabilen Isotope besitzt und liefert aufgrund seiner kurzen Halbwertszeit einen zeitabhängigen Einblick in die Sternentwicklung. In dieser Arbeit wurden hochgeladene Rutheniumionen in der Heidelberger Elektronenstrahl Ionen Falle produziert und untersucht. Das von den angeregten Ionen emittierte Fluorenszenzlicht wurde mit Hilfe eines Czerny-Turner Monochromators aufgenommen. Die 53 gemessenen optischen Linien der Ladungszustände Ru^{9+} bis Ru^{18+} wurden mit theoretisch berechneten Werten verglichen, was eine vorläufige Bestimmung von 30 Übergängen ermöglicht hat.

Contents

1 Introduction

Since the first astronomical observations, stars have always played a major role in giving us insight into the evolution of the Universe. A star is a spherical body consisting of plasma, held together by its own gravity, while a gravitational collapse is prevented by the pressure resulting from its radiation. Over the course of its lifetime a star undergoes significant changes, including variations in its size and radiation. The emitted spectrum of a star thus yields information about the evolutionary stage of the star and the elements of which it is composed. The stellar evolution, describing the birth, life and death of a star is understood in principle, but there are still many unanswered questions, one of which is the nucleosynthesis of trans-iron elements (elements with a higher atomic number Z than iron) in stars. There are multiple nucleosynthesis processes occurring in a star, but the most prominent one is nuclear fusion, where two nuclei are merged to form a new element of a higher Z. This process, however, cannot produce heavier elements than iron, since iron has the highest binding energy per nucleon. The trans-iron elements are products of the s-process (slow neutron capture process) in the intershell region of the star, where they are hidden from our telescopes. However due to high radiation pressure, the intershell elements can reach the surface and thus appear in the spectrum of the star. Spectral data of white dwarfs such as RE 0503-289 show high abundances of trans-iron elements, as shown in figure 1.1.

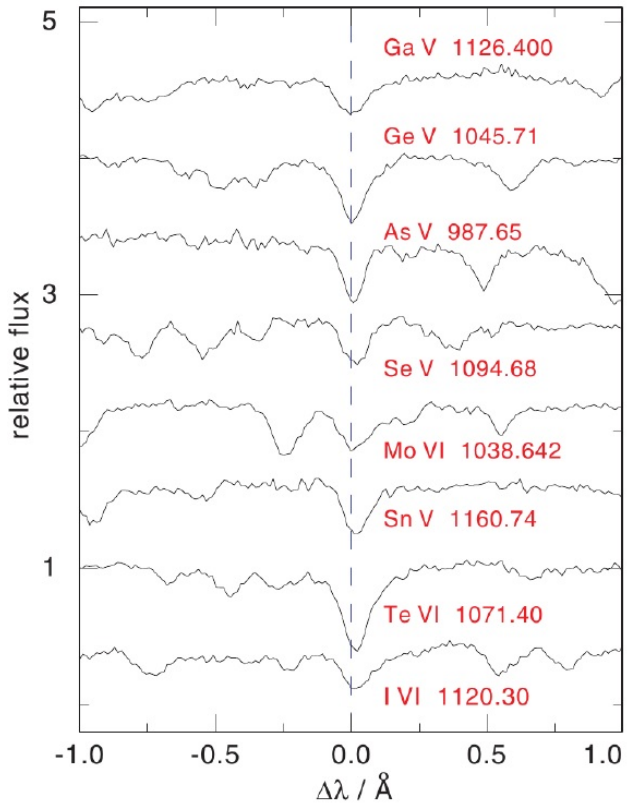

Figure 1.1: Spectral data of the star RE 0503-289 taken by the Far Ultraviolet Spectroscopic Explorer (FUSE) satellite show contributions from ionized trans-iron elements. Image taken from [1].

One of the trans-iron elements is technetium (Z=43), the lightest unstable element with a half-life of 210 000 years. The detection of technetium will therefore result in a better comprehension of the trans-iron elements synthesis and of stellar evolution in general.

Technetium was first discovered in the atmosphere of red giants by P. Merrill in 1952 [2], which leads to the assumption that it could be present in a star whenever other products of the s-process are detected. The current goal in this field of research is to find traces of technetium in RE 0503-289 and similar stars [3]. However to forward this project, spectral data of the trans-iron elements is needed, as so far only very few of the heavier elements have been investigated beyond their lowest charge states, which is shown in figure 1.2.

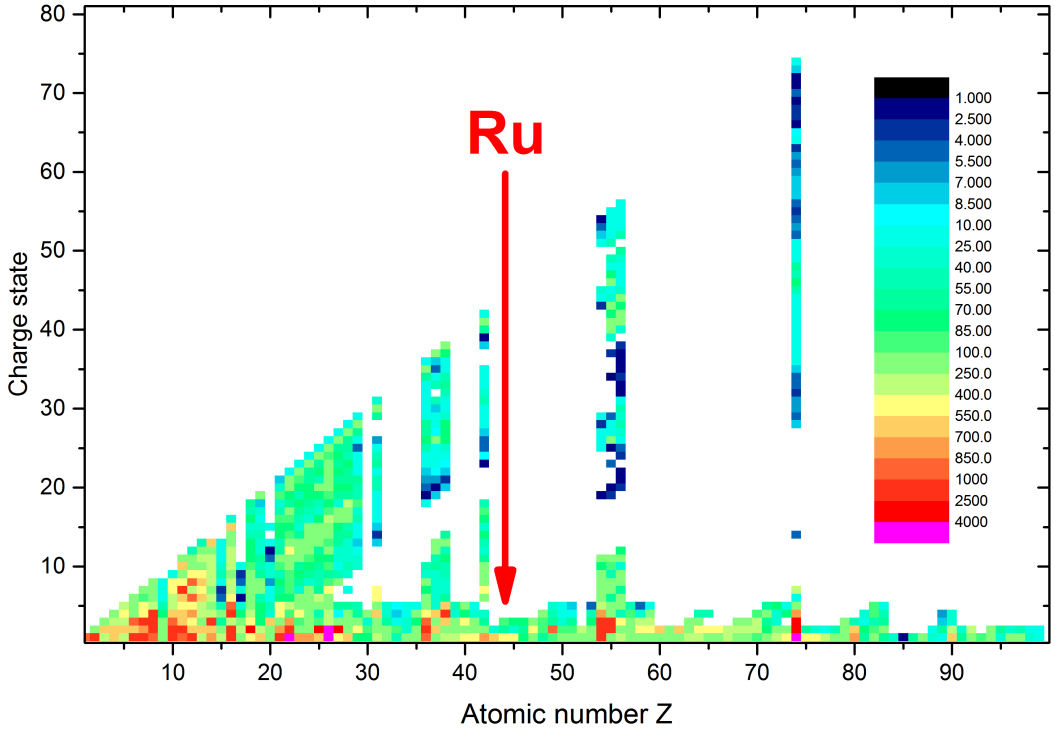

Figure 1.2: Overview of the number of measured spectral transitions for ions with atomic number Z, according to the NIST atomic spectra database [4]. The magenta rectangles specify a charge state of a specific element which has more than 4000 measured transitions, while the white areas represent charge states for which no data has been collected so far.

To obtain this spectral data the apparatus of choice is the electron beam ion trap (EBIT). In an EBIT, highly charged ions (HCI) can be produced and trapped, by means of a magnetically compressed electron beam. However investigations of technetium with an EBIT are not yet possible since the radioactive nature of the element involves complex alterations of the experimental setup. Therefore in this work, ruthenium (Z=44) is investigated, as it has a similar atomic structure compared to technetium. The obtained ruthenium data can then be used to predict the emission properties of technetium through extrapolation [5] with the spectral data of molybdenum (Z=42), which is already available. The experiment was performed at the Heidelberg EBIT (HD-EBIT) and comprised the investigation of Ru^{9+} to Ru^{18+}.

2 Theory

In this chapter, an introduction to atomic physics is presented. The focus lies on the laws of atomic physics necessary to describe the processes taking place in an EBIT and perform computational methods to predict the electronic structure of atoms. However a full overview of atomic physics will not be featured in here. For a more detailed approach one can refer to literature such as Kuckuck or Demtröder [6, 7].

2.1 One-Electron systems

The starting point is the simplest atomic system consisting of an electron and a positively charged nucleus. This system can be described by a wave function $\Psi(\mathbf{r}, t)$, which can be found by solving the Schrödinger equation

$$i\hbar\frac{\partial}{\partial t}\Psi(\mathbf{r}, t) = H\Psi(\mathbf{r}, t), \tag{2.1}$$

with the Hamiltonian

$$H = \frac{-\hbar^2}{2\mu}\Delta + V(\mathbf{r}, t), \tag{2.2}$$

where $\mu = \frac{m_e M}{m_e + M}$ is the reduced mass with the electron rest mass m_e and M the mass of the nucleus and $\hbar = h/2\pi$ the reduced Planck constant. The electromagnetic interaction between the nucleus and the electron corresponds to the Coulomb-potential which is described by

$$V(\mathbf{r}) = -\frac{Ze^2}{4\pi\epsilon_0|\mathbf{r}|}, \tag{2.3}$$

with ϵ_0 the electric constant, Ze as the nucleus charge and $|\mathbf{r}|$ as the distance between the nucleus and the electron. Considering the time independence of the Coulomb-potential, equation (2.1) simplifies $H\Psi(\mathbf{r}) = E\Psi(\mathbf{r})$. Hence the Schrödinger equation can be written as

$$\left[\frac{-\hbar^2}{2\mu}\Delta - \frac{Ze^2}{4\pi\epsilon_0|\mathbf{r}|}\right]\Psi(\mathbf{r}) = E\Psi(\mathbf{r}). \tag{2.4}$$

A complete approach to the solution is not featured here and can be found in [6], thus only the final solution is presented. The wave function is expressed in spherical coordinates due to the symmetry of the system and consists of a radial function and a spherical harmonic:

$$\Psi(r, \vartheta, \phi) = R_{n,l}(r) Y_m^l(\vartheta, \phi) \tag{2.5}$$

with the main quantum number $n = 0, 1, 2, ...$, the angular quantum number $l = 0, 1, 2, ..., n-1$ and the magnetic quantum number $m = -l, -(l-1), ..., (l-1), l$. The resulting discrete energies E_n are given by

$$E_n = -\frac{\mu c^2 (Z\alpha)^2}{2} \frac{1}{n^2} \tag{2.6}$$

with $\alpha = \frac{e^2}{4\pi\epsilon_0 \hbar c}$ the fine-structure constant. They depend on the main quantum number n, while the quantum numbers l and m have no influence on the energies in this approach, which is why one energy can have multiple possible solutions resulting in a degenerate state.

An electron can perform transitions between the energy levels by emitting or absorbing energy as for example in the from of a photon. As the photon energy is equivalent to the energetic difference between the two levels, information about the atomic structure can be obtained through measuring it by means of spectrometry.

2.2 Fine structure

The previous approach to the hydrogen-like system is already very accurate. However measurements with high resolution show small energy splittings in the spectral lines resulting in an observation of a doublet instead of a single line known as the fine structure splitting. This is caused by the electron spin $\mathbf{s}$ and the resulting spin magnetic moment of the electron, which was observed in the Stern-Gerlach experiment

$$\boldsymbol{\mu}_s = -g_s \frac{\mu_B}{\hbar} \mathbf{s}, \tag{2.7}$$

where $\mu_B = e/2m_e$ is the Bohr magneton and $g_s \approx 2$ the electron g-factor. The associated spin quantum number is $s = \frac{1}{2}$.
As the electron is moving through the electric field of the nucleus, a magnetic field

is created around the electron which can be expressed as

$$\mathbf{B} = \frac{\mu_0 Ze}{8\pi|\mathbf{r}|^3 m_e}\mathbf{l} \tag{2.8}$$

with $|\mathbf{r}|$ the distance between the electron and nucleus, μ_0 the magnetic constant and $\mathbf{l}$ the electrons orbital angular momentum. The resulting interaction between the spin electron momentum and the magnetic field $\mathbf{B}$ is responsible for the line splitting and is called the spin-orbit interaction.

To obtain the splitting energy the Hamiltonian from (2.2) has to be adjusted accordingly.

$$H = H_0 - \mu_s \cdot \mathbf{B} = H_0 - g_s \mu_B \frac{\mu_0 Ze}{8\pi\hbar|\mathbf{r}|^3 m_e}(\mathbf{s}\cdot\mathbf{l}). \tag{2.9}$$

With the introduction of the total angular momentum $\mathbf{j} = \mathbf{l} + \mathbf{s}$ and use of the relation $(\mathbf{s}\cdot\mathbf{l}) = \frac{1}{2}[\mathbf{j}^2 - \mathbf{l}^2 - \mathbf{s}^2]$ the splitting energy can be expressed relative to the established energy levels E_n as

$$\triangle E_{FS} = E_n \frac{Z\alpha^2}{n \cdot l(l+1)}. \tag{2.10}$$

2.3 Many-electron systems

For a system consisting of a nucleus and more than one electron, an analytical approach is no longer possible. By adding more electrons to the system they not only interact with the nucleus but also with each other. To take this into consideration the repulsive contribution H_{RE} of the other electrons is added to the Hamilton operator.

$$H = H_0 + H_{RE} = \sum_{i=1}^{N}\left(-\frac{\hbar^2}{2\mu}\Delta - \frac{Ze^2}{4\pi\epsilon_0|\mathbf{r}_i|}\right) + \sum_{i<j=1}^{N}\frac{e^2}{4\pi\epsilon_0|\mathbf{r}_{ij}|} \tag{2.11}$$

Here N is the number of electrons, $\mathbf{r}_i$ the position of the i-th electron and $\mathbf{r}_{ij}$ the distance between the i-th and j-th electron. The potential is thus no longer spherically symmetric, but depends on the angle between the two radius vectors of the electrons. A separation of the wave function into a radial and angular part as performed in section 2.1 is no longer possible. Instead an approximation can be made

by using an iterative method, which is introduced in the next subsection.

2.3.1 Hartree-Fock method

The Hartree-Fock method describes an N-electron wave function as a product of one-electron wave functions. As electrons are fermions, the N-electron wave function must be antisymmetric under exchange of electrons in order to satisfy the Pauli exclusion principle. This principle states that two fermions cannot exist in the same quantum state. Therefore the N-electron wave function is approximated by the Slater determinant

$$\Psi(\mathbf{r}_1, \mathbf{r}_2, ..., \mathbf{r}_n) = \frac{1}{\sqrt{n!}} \begin{vmatrix} \psi_1(\mathbf{r}_1) & \psi_2(\mathbf{r}_1) & \dots & \psi_n(\mathbf{r}_1) \\ \psi_1(\mathbf{r}_2) & \psi_2(\mathbf{r}_2) & \dots & \psi_n(\mathbf{r}_2) \\ \vdots & \vdots & \ddots & \vdots \\ \psi_1(\mathbf{r}_n) & \psi_2(\mathbf{r}_n) & \dots & \psi_n(\mathbf{r}_n) \end{vmatrix} \tag{2.12}$$

with the one-electron wave functions $\psi_i(\mathbf{r}_i)$. By utilizing the variational method one can obtain the Hartree-Fock wave function and energy of the system. The method calculates the energy eigenvalues $E_i^{(0)}$ of each wave function $\psi_i^{(0)}$ and constructs a potential for a specific wave function ψ_i of the i-th electron. With this new potential the eigenvalues and wave functions $E_i^{(1)}$ and $\psi_i^{(1)}$ are calculated again and compared to the previously calculated $E_i^{(0)}$ and $\psi_i^{(0)}$. This is repeated until the energy eigenvalues converge to a minimum value, because it is assumed that the true energy eigenvalues of the wave function are always lower than the values obtained by the approximation.

2.3.2 LS- and jj coupling

So far, the contribution of the spin-orbit interaction mentioned in section 2.2 has been neglected in this approach. Therefore the coupling term H_C is added.

$$H_C = \sum_{i=1}^{N} \frac{1}{2m^2c^2} \frac{1}{|\mathbf{r}_i|} \nabla V(\mathbf{r}_i)(\mathbf{s}_i \cdot \mathbf{l}_i) \tag{2.13}$$

To determine the Hamiltonian $H = H_0 + H_{RE} + H_C$ one has to consider the two possible cases $|H_{RE}| \ll |H_C|$ and $|H_{RE}| \gg |H_C|$ depending on the examined atom. The first case applies to light atoms and is solved by considering the LS coupling,

while the second case applies to heavier atoms and is solved with the jj coupling.

In the case of LS coupling the coupling energies between the orbital angular momenta of the electrons and between the electron spins are higher than the coupling energies between the orbital and spin angular momenta of each individual electron. This leads to the coupling of the individual orbital angular momenta to the total orbital angular momentum $\mathbf{L} = \sum_{i=1}^{N} \mathbf{l}_i$, and a coupling of the spins to the total spin $\mathbf{S} = \sum_{i=1}^{N} \mathbf{s}_i$. Finally this results in a coupling of $\mathbf{L}$ and $\mathbf{S}$ to form the total angular momentum $\mathbf{J} = \mathbf{S} + \mathbf{L}$. For heavy atoms the energy of the orbital and spin angular momenta of the individual electrons becomes stronger. The orbital and spin angular momenta couple for each electron individually and form the total angular momentum $\mathbf{j} = \mathbf{s} + \mathbf{l}$ of a single electron. These momenta then couple to form the total angular momentum $\mathbf{J} = \sum_{i=1}^{N} \mathbf{j}_i$.

2.4 Computational methods

In this work theoretical calculations have been performed using the flexible atomic code (FAC) developed by M. F. Gu [8], in order to compare them with the measured data. The FAC modules were used to calculate the energies of the fine-structure levels of the investigated ions as well as the transition rates in between those levels. Additionally, the cross sections of excitation induced by electron collisions have been calculated allowing the generation of synthetic spectra using the collisional radiative model (CRM). The CRM is used to better interpret emission spectra from plasmas. The model usually considers many atomic processes that are taking place in plasmas, excluding charge exchange. For more information about the CRM model one can refer to a description of the model made by H. K. Chung [9]. However in this work the only considered process is electron impact excitation. The reasoning behind this is the given environment of the trapping region of the EBIT. The charge state distribution is assumed to be dominated by the investigated charge state, which will later be shown in this work. This allows the exclusion of excitations resulting from recombination from higher charge states. The effects of electron impact ionization and recombination are also neglected as the ionization caused by electron collision is assumed to mainly produce the investigated ions in their ground state. Ultimately, this allows the formulation, as presented in [5], of the rate equation describing the

time dependence of the population n_i of the state i as follows

$$\frac{dn_i}{dt} = \sum_{i>j} n_e C(\sigma_{ij}^{EIE}, E_e) - \sum_{i<j} n_e C(\sigma_{ij}^{EIE}, E_e) - \sum_{i>j} n_i A_{ij} + \sum_{i<j} n_j A_{ji}. \quad (2.14)$$

Here the first term represents the electron impact excitation from a less energetic state j to a higher state, while the second term describes the opposing process of electron impact de-excitation, from a higher energetic state j. Both terms depend on the electron impact excitation cross section σ^{EIE}, the energy of the electrons E_e and their density n_e. The last two terms account for the spontaneous decay from the energetically higher state i to the state j in the case of the third term and for the spontaneous decay from the state j to the less energetic state i. They are described by the Einstein coefficients A_{ij} and A_{ji} respectively.

3 Experimental Setup

This chapter addresses the setup of the Heidelberg electron beam ion trap (HD-EBIT), which was used to obtain the experimental data for this thesis. Furthermore the properties of the electron beam as well as the optical setup will be discussed.

3.1 Electron Beam Ion Trap

The EBIT is a device to produce, trap and excite highly charged ions (HCI) in order to study them. The following sections will elaborate how this is accomplished and highlight the characteristics of the HD-EBIT.

3.1.1 Working principle

Neutral atoms injected into an EBIT are ionized via electron impact ionization by a magnetically compressed electron beam. The electrons are emitted by an electron gun, accelerated towards the central drift tube and eventually dumped in the collector. The trapping region located between the gun and the collector consists of several drift tubes with a connection to the injection system. A schematic representation of an EBIT is displayed in figure 3.1. Due to their positive charge, the ions are trapped radially by the negative space charge of the electron beam. To trap them in the axial direction, a specific trapping potential can be created by applying voltage to the drift tube electrodes. The now trapped ions are ionized even further until the needed ionization energy exceeds the energy of the electron beam.

Additionally, the beam is exciting the ions leading to spontaneous emission of photons, which in turn can be observed through observation slits in the central drift tube.

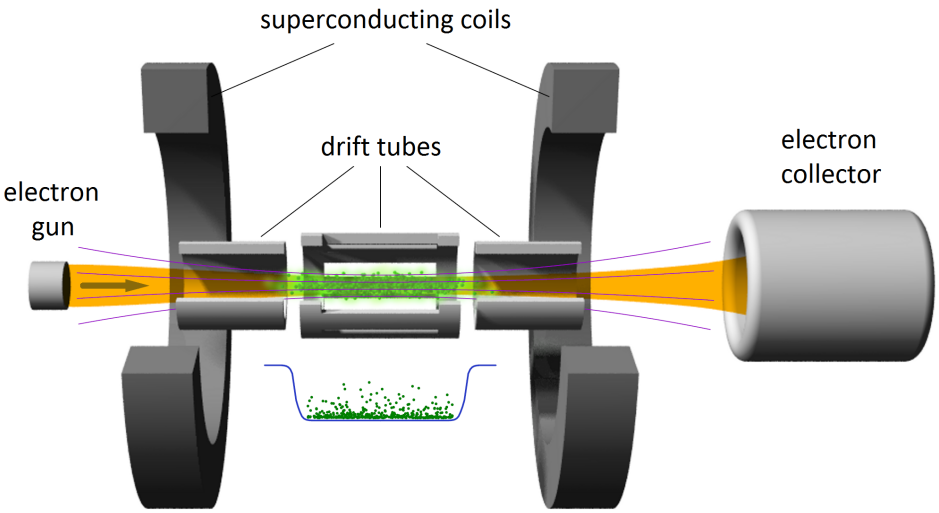

Figure 3.1: Schematic of an Electron Beam Ion Trap. The ions (green) are trapped in radial direction by the negative space charge of the electron beam (orange) which is compressed by the magnetic field (purple) of the superconducting coils and trapped in axial direction by the potential well (blue) set to the drift tubes. Image taken and altered from [10].

3.1.2 The Heidelberg-EBIT

The cross section of the Heidelberg EBIT is presented in figure 3.2. The electron gun employed in the HD-EBIT features a barium-wolfram cathode emitting electrons through the Edison effect. Due to the high temperatures necessary for electron emission, small amounts of barium and wolfram are also emitted. Over time, these ions can dominate the trap contents, which can be prevented by regularly emptying the trap during the experiment. This is accomplished by shortly inverting the trapping potential, a process that is referred to as dumping.

The applied potential between the cathode and the anode accelerates the electrons towards the anode. To prevent any collision with the anode, the electrons are collimated by a focusing anode, which is set to a lower potential than the anode. Additionally, to prevent unwanted interactions with the magnetic field generated by the main magnet located at the drift tubes, a bucking coil is installed around the electron gun for compensating the field. Thereby, the electrons passing through the

anode enter the drift tubes in form of a collimated beam. The HD-EBIT features nine drift tubes with individually adjustable potentials to create a custom trapping potential.

The main magnet, consisting of two superconducting coils in Helmholtz configuration, produces a magnetic field of 8 T which compresses the electron beam along the drift tubes to a diameter of approximately 50 µm. The coils are cooled to temperatures slightly above 4 K using liquid helium.

Finally, after passing through the drift tubes the electron beam is dumped in the collector. This is achieved with the collector coil, which compensates the compression of the beam induced by the main magnet, and with the suppressor electrode mounted in front of the collector. These measures help to expand the electron beam, causing the electrons to hit the inner surface of the collector where the kinetic energy of their impact is discharged with the water cooling system of the collector. To ensure that no electron is able to pass the collector, the extractor electrode, whose potential is set lower than the cathode potential, is installed in the rear of the collector. This extractor can also be used to extract ions from the EBIT to perform further measurements.

In order to be able to perform optical spectrometry, the light can pass through a slit in the central drift tube perpendicular to the electron beam and further passes through two quartz lenses before leaving the EBIT through a quartz window at the outer vacuum barrier, in front of which the optical setup is mounted as shown later in figure 3.3.

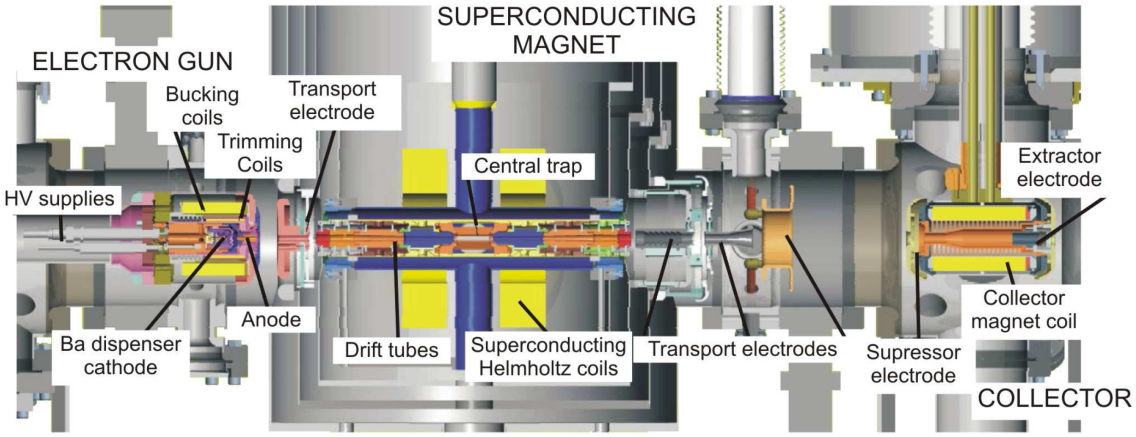

Figure 3.2: Cross section of the Heidelberg-EBIT. The electron beam traverses the EBIT starting at the electron gun then passing through the drift tubes, while being compressed by the magnetic field of the superconducting magnets and ending in the collector. Image taken from [11]

3.1.3 Electron beam

The energy of the electron beam inside the EBIT is an important parameter as it directly affects the charge state of the ions inside the trap. It is estimated by the potential difference between the cathode and the central drift tube

$$E_e = e(-U_c + U_{\mathrm{DT9}}). \tag{3.1}$$

In this expression, however, the influence of the space charge of the electron beam is neglected. An approximation of the space charge in the center of the central drift tube is given by [11]

$$U_{\mathrm{SC}}[V] \approx \frac{30 \cdot I_e[A]}{\sqrt{1 - \left(\frac{E_e[keV]}{511} + 1\right)^{-2}}} \left(ln \left(\frac{r_H}{r_{\mathrm{DT9}}} \right)^2 - 1 \right) \tag{3.2}$$

with the electron beam current I_e, the previously calculated electron beam energy E_e, the inside radius of the central drift tube r_{DT9}=5 mm and r_H the Hermann radius of the electron beam. In the Hermann model [12] this radius is defined as the

radius containing 80 % of the electrons of the beam and can be calculated by

$$r_H = r_B \sqrt{\frac{1}{2} + \sqrt{\frac{1}{4} + \frac{8 m_e k_B T_c r_c^2}{e^2 B^2 r_B^4} + \frac{B_c^2 r_c^4}{B^2 r_B^4}}} \tag{3.3}$$

with the cathode temperature T_c, the magnetic field strength at the cathode B_c, the magnetic field strength at the central drift tube B, the cathode radius r_c,the Brillouin radius r_B the electron charge e, electron mass m_e and the Boltzmann constant k_B. The Brillouin radius is given by

$$r_B = \sqrt{\frac{m_e I_e}{\pi \epsilon_0 \upsilon e B^2}} \tag{3.4}$$

where υ is the axial electron velocity. The Herrmann radius has been calculated by using values similar to those used in this work and is approximately 25 µm [5]. The obtained space charge is also partially compensated by the positive space charge of the ion cloud. However, the contribution of the positive space charge depends on the number and charge distribution of the ions which cannot be estimated. Thus, the space charge correction is estimated from previous experimental experience [13] [5].

3.2 Optical Setup

This section is divided into three parts covering the CCD detector, the Czerny-Turner spectrometer and the image rotation system including the calibration setup. The complete optical setup that has been used in this experiment is shown in figure 3.3. Before the light of the ion cloud reaches the first component of this setup (the image rotation system) it passes two plano-convex lenses inside the vacuum chamber of the EBIT and gets projected to a quartz window on the outer vacuum barrier.

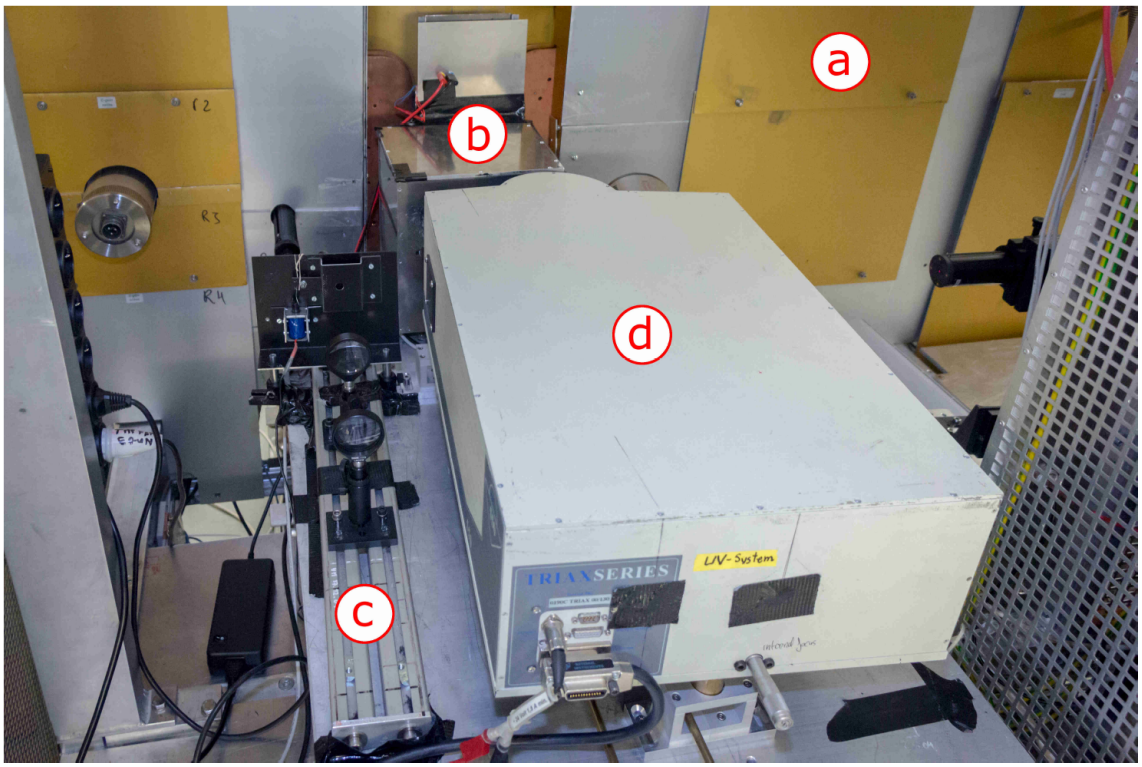

Figure 3.3: The optical setup equipped at the HD-EBIT. Light generated in the EBIT (a) first enters the image rotation system (b) where it is rotated and then projected onto the entrance slit of the spectrometer (d). (c) is the optical bench with the mounted calibration lamp and converging lens. Image taken from [14]

3.2.1 CCD detector

A charge-coupled device (CCD) composed of 2048×512 pixels was used for recording the diffracted light leaving the spectrometer. The 2048 pixels lie on the dispersive plane and are thus used to obtain the wavelength information of the recorded spectrum, while the others are needed for image corrections. To reduce the readout noise, a binning in 8 stripes is applied to the vertical plane resulting in 8 areas with 2048×64 pixels. The CCD is cooled with a Peltier element to reduce thermal noise. This is necessary since the measured lines often show low intensities, requiring long exposure times. The drawback of long exposures is the increase of impurities on the obtained image due to cosmic rays hitting the CCD constantly throughout the exposure time. However, these can be removed in later stages of data analysis.

3.2.2 Spectrometer

The spectrometer used in this work is a Czerny-Turner monochromator. A schematic of the spectrometer is shown in figure 3.4. The light entering the spectrometer through the entrance slit (A) is collimated onto the grating (G) by the concave mirror (S1). The diffracted light is then collected by a second concave mirror (S2) and refocused onto the detector (D).

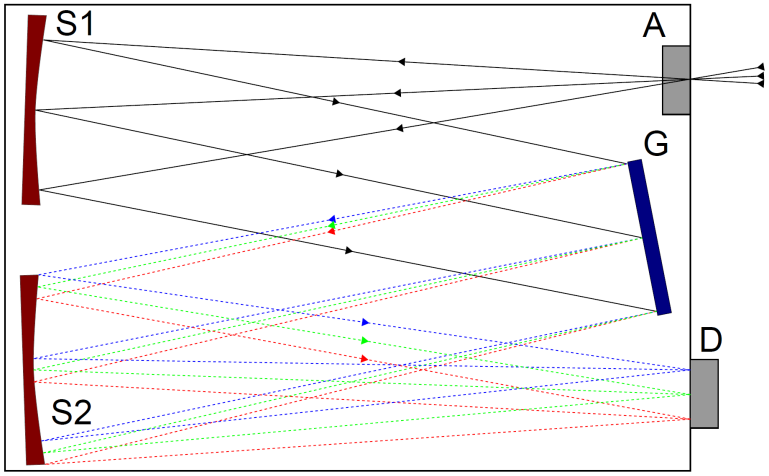

Figure 3.4: Schematic of the Czerny-Turner spectrometer. Image taken from [14].

The grating installed in the spectrometer is a blazed reflective grating. It features sawtooth-shaped grating lines, which form a step structure. The steps are slanted at the blazed angle θ_b with respect to the grating surface. A blazed grating is used to optimize the diffraction efficiency of a certain wavelength λ, which is shown in figure 3.5. To analyze a region around the wavelength λ the grating has to be rotated so that the grating equation [15]

$$\sin(\alpha) + \sin(\beta) = \frac{n\lambda}{g} \tag{3.5}$$

is satisfied. Here, α is the angle of incidence, β is the angle of reflection with respect to the grating normal, n is the diffraction order and g is the line spacing of the grating. The grating used in this work features a line spacing of 300 lines per mm.

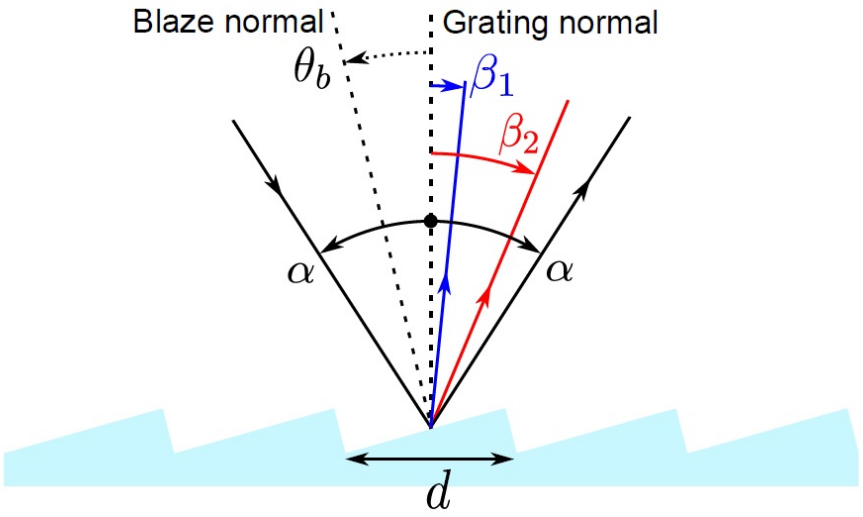

Figure 3.5: Scheme of a blazed reflective grating. With the given blaze angle θ_b the blue light reflected under the angle β_1 has the same angle of incidence β_1 with respect to the blaze normal. This optimizes the diffraction efficiency of the blue light. Image taken from [5].

3.2.3 Image rotation system and calibration

As the ion cloud trapped inside the EBIT has a horizontal expansion (approximately 40×0.5 mm^2), the light emitted by the ions must be rotated before entering the vertical entrance slit of the spectrometer in order to maximize the luminous intensity of the measurement. To achieve this the light of the ion cloud is directed into the image rotation system shown in figure 3.6. The system consists of three mirrors and two lenses of which the first mirror (a) and the last lens (e) are adjustable to ensure an optimal projection onto the entrance slit of the spectrometer.
An argon-iron-hollow-cathode calibration lamp is used in order to calibrate the obtained spectra. The Ar-Fe-source is mounted on an optical bench (c) alongside the spectrometer. The light is focused into a glass fiber using a converging lens. The glass fiber then directs the light onto a diffusive reflector, whose position can be adjusted in order to shine calibration light or light from the ion cloud into the spectrometer. To further ensure that no calibration light can falsify the ion cloud spectra, a shutter is mounted in front of the glass fiber which blocks the optical path of the calibration light during acquisitions of the ion cloud. This setup can be operated by remote control allowing an automated measurement with the suitable scripts and a prior optimization of the image rotating system.

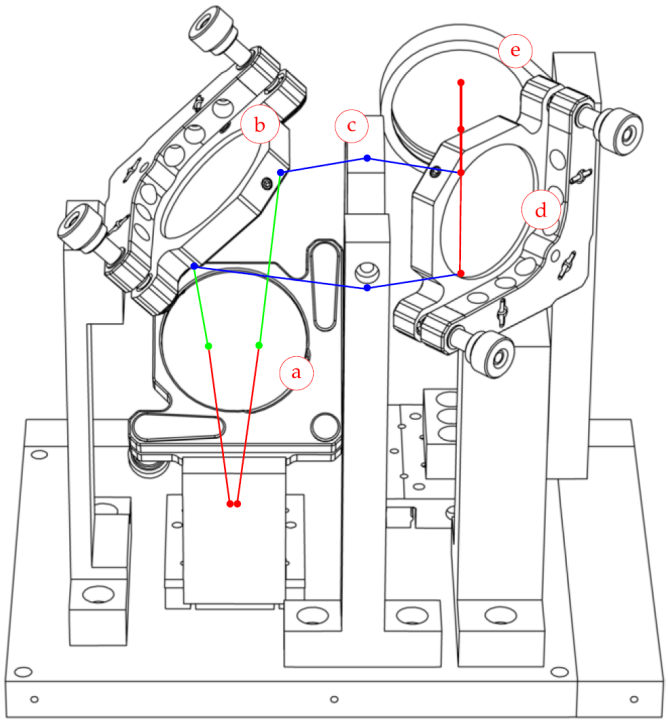

Figure 3.6: Image rotation system as viewed from the HD-EBIT window. (a), (b) and (d) are mirrors and (c) and (e) are lenses. (a) and (e) can be adjusted to change the horizontal position and the focus of the image. Image taken from [16].

4 Performing the experiment

This chapter describes the individual work steps performed during the experiment and mentions the different settings applied to the EBIT and the optical setup.

4.1 Injection

In the HD-EBIT the element of interest is injected into the trap center in form of a molecular beam. To favor this method, a volatile compound containing ruthenium had to be found. The compound Tris(2,2,6-tetramethyl-3,5-heptanedionato)ruthenium(III) (C33H57O6Ru) satisfies these requirements. The binding energies of the molecule are surpassed by the electron beam energy, hence the bonds are broken once the molecule comes in contact with the beam. The other components besides ruthenium, hydrogen, carbon and oxygen are lighter than ruthenium and thus leave the trapping region as they can only reach low charge states. The remaining ion cloud is also cooled during this process, which is called evaporative cooling. The probe vessel is connected to the first injection stage via a needle valve, used to regulate the flow of gas into the first stage. A small aperture is leading to the second injection stage, where the gas needs to pass one more aperture to reach the central drift tube. In order to inject a sufficient amount of the molecule the probe vessel is heated to 80 °C during the measurements. The resulting pressures in the injection stages are $p_{\mathrm{inj1}} = 7 \cdot 10^{-7}$ mbar in the first stage and $p_{\mathrm{inj2}} = 2 \cdot 10^{-8}$ mbar in the second stage.

4.2 Optimizing the electron beam

The first step is to optimize the electron beam by adjusting the potential of the focus electrode and the position of the electron beam through a slight altering of the position of the electron gun. The currents measured on the anode and the suppressor electrode are indicators of the stability and straightness of the electron beam. These

currents should be minimized, while maximizing the collector current. When the currents are showing only small fluctuations the auto focus of the electron beam should be activated to maintain a stable electron beam during the measurements. In the course of this work the electron beam has the properties I_e=40 mA, E_e=520 eV for the higher charge states and I_e=8 mA, E_e=170 eV for the lower charge states. The stated electron beam energies are the initial beam energies, which are increased stepwise during the experiment.

4.3 Optimizing the trapping potential and optical setup

After applying a trapping potential to the drift tubes, the ruthenium compound can be injected into the central drift tube to obtain the first spectrum. In the following, the trapping potential as well as the electron beam energy can be modified to ensure the highest possible intensity for the observed light. The applied trapping potentials are 20 V - 70 V - 20 V for the higher charge states and 10 V - 20 V - 10 V for the lower charge states, where the central voltage is applied to the central drift tube (DT9) and the outer voltages are applied to the drif tubes in front and behind DT9. To ensure that the obtained light originates from the injected ruthenium the spectrum is recorded with a closed injection after inverting the trap. Now the optical setup needs to be optimized for the measured wavelength. A bright line in the middle of the spectrum is chosen to determine the optimal positions of the focus lens and the first mirror of the image rotation system in order to project and focus the light of the ion cloud onto the entrance slit of the spectrometer. The focus is optimized when the intensity of the line reaches a maximum and the full width at half maximum (FWHM) of the line is minimal. To project the light on the middle of the entrance slit, the peak position of the line is measured with a fully opened entrance slit (2 mm) and the slit size which was used during the following ion cloud acquisition, while changing the position of the mirror. The entrance slit sizes were 70 µm for the high energy measurements and 200 µm for those with lower energies. This is repeated until the shift of the peak position between the two applied slit sizes is approximately one pixel. The optimization of the optical setup is performed before every measurement with a different wavelength range.

4.4 Data acquisition

The measurements in this work are performed in the form of energy scans, meaning that the electron beam energy is raised for a fixed amount, by applying a higher voltage to the drift tube platform after each acquisition. For the measurements of the lower charge states E_e is raised from 170 eV to 400 eV in steps of 5 eV and for the higher charge states from 520 eV to 900 eV in steps of 10 eV. In order to cover the full optical range of the emission spectrum each energy scan is performed 3 times with different overlapping wavelength ranges. Hence 6 energy scans have been performed in total, while a background spectrum was recorded for each scan as well as a calibration spectrum before and after each step of the scan. The background spectra were obtained with a inverted trap to correct the ion cloud measurements for possible stray light inside the EBIT. The acquisition time for the individual spectra of each energy step as well as for the background spectra was 30 minutes whereas the calibration spectra had an acquisition time of 3 minutes.

5 Analysis

5.1 Cosmic removal

The cosmic rays mentioned in 3.2.1 consist of highly energized particles hitting molecules in the atmosphere of the earth. Secondary particles such as muons produced during the collision reach the surface of the earth and eventually strike the CCD camera, generating a strong signal in the affected pixels. These pixel errors, referred to as cosmics had to be removed from all of the recorded spectra including the calibration and background measurements. This process is shown exemplarily in figure 5.1, displaying a ruthenium spectrum before and after cosmic removal is applied.

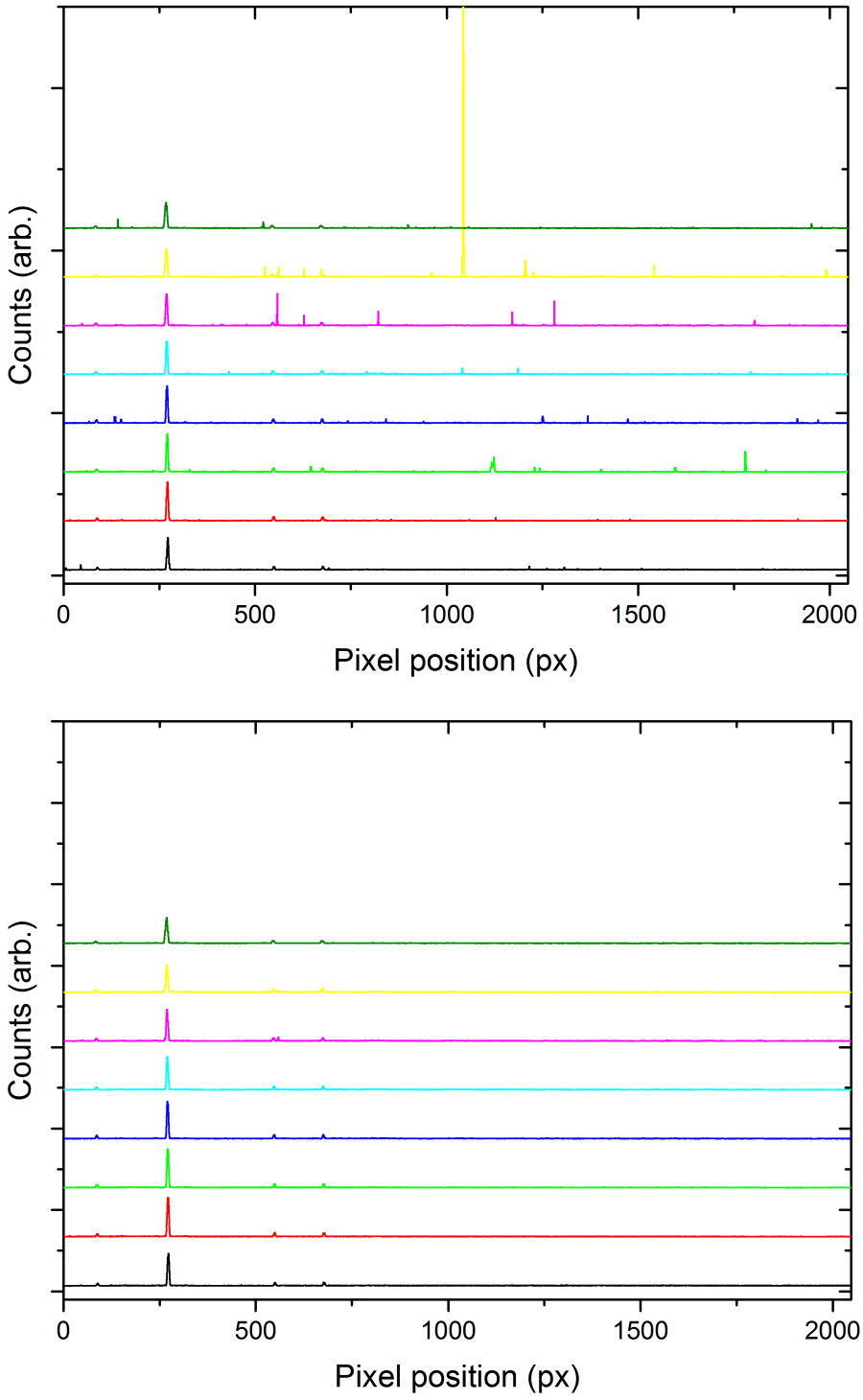

Figure 5.1: The spectrum of Ru^{17+} in the range of 290 to 470 nm is shown before (above) and after the cosmic removal algorithm is applied (below). Constants are added to the intensities of each bin for a better visualization

To accomplish this task the cosmic-ray rejection algorithm written by Wojtek Pych was implemented in python [17]. The recorded image is divided into overlapping sub-frames for each of which a histogram of the count distribution is constructed. As the cosmic signal is characterized by a high amount of counts, a gap can be found in the histogram when the sub-frame features a cosmic signal. If this gap exceeds a selected threshold, the pixels with counts above this gap are removed from the image. Setting this threshold too low results in unwanted removal of the ion signal, while setting it too high may leave a small amount of cosmics uncorrected.

5.2 Line straightening

The CCD features a slight rotation with respect to the diffracted spectral lines of the ion cloud, which can be seen in figure 5.2 showing an uncorrected line of the recorded spectrum of Ru^{17+}.

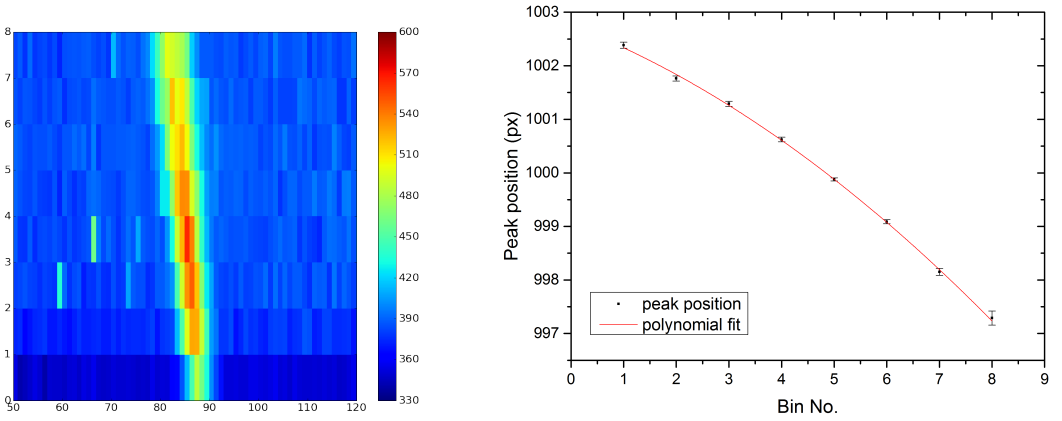

Figure 5.2: (left) Raw data of the recorded 297 nm line of Ru^{17+} showing a noticeable horizontal shift along the vertical axis. (right) parabolic fit of the peak positions plotted against their bin number.

This problem is solved using a line straightening procedure introduced in [18]. First the horizontal pixel position of a selected calibration line is determined in each of the 8 bins of the obtained calibration spectrum with a Gaussian fit. The peak positions and their respective errors are then plotted against their bin number and a parabolic fit is applied as shown in figure 5.2. Ultimately, the bins are aligned according to the obtained parameters. In a last step the bins from number 2 to number 6 are jointed by calculating their arithmetical mean to produce a two di-

mensional spectrum. The bins 1,7 and 8 are excluded to account for the optical aberration known as coma.

5.3 Calibration

For each of the three measured wavelength ranges, one calibration spectrum was taken, of which the pixel positions of the calibration lines were fitted with a Gaussian. The measured calibration lines and their Gaussian fits of the second wavelength range, reaching from 290 to 470 nm, are shown in figure 5.3. Most of the lines of the argon-iron lamp were identified with the help of previous measurements [19] [18] and the National Institute of Standards and Technology (NIST) spectral database. The pixel positions of the identified lines and their fit errors are plotted as x-values together with the respectively assigned wavelength obtained from the NIST data base as y-values. This plot is then fitted with a parabolic function as demonstrated in figure 5.3. Here the errors of the wavelength are neglected since they are small compared to the fit uncertainties of the pixel positions. The fit results have been evaluated for each calibration by creating a residual plot as shown in figure 5.3. Also for every calibration a confidence band for an uncertainty of 68 % $\approx 1\sigma$ has been calculated. For the following analysis the width of the confidence band at the corresponding position will be serving as the calibration error for most of the identified lines. To ensure an optimal calibration for each line of the ion spectrum, every pair of calibration spectra, obtained at the beam energy where this line reached maximum intensity, was fitted using the previously received reference wavelengths. This was performed with a python program, which proceeded to match them with the respective reference lines of the NIST data base. The final fit utilizes only the reference lines with a deviation from the fit lower then a previously set threshold. In a last step the arithmetical mean of each pair of calibration functions is calculated and applied to the respective ion spectrum.
By examining the confidence band in figure 5.3 one can observe the decreasing fit accuracy at the edges of the spectrum. In the case of the first two calibration ranges the accuracy is further impaired as only very few reference lines could have been found in the lower wavelength range of the calibration spectrum. This is of particular importance considering that the obtained spectra are connected, which leads to discrepancies between the calibrations in the overlap. An assembled calibration spectrum of the three investigated wavelength regions, displaying the overlapping

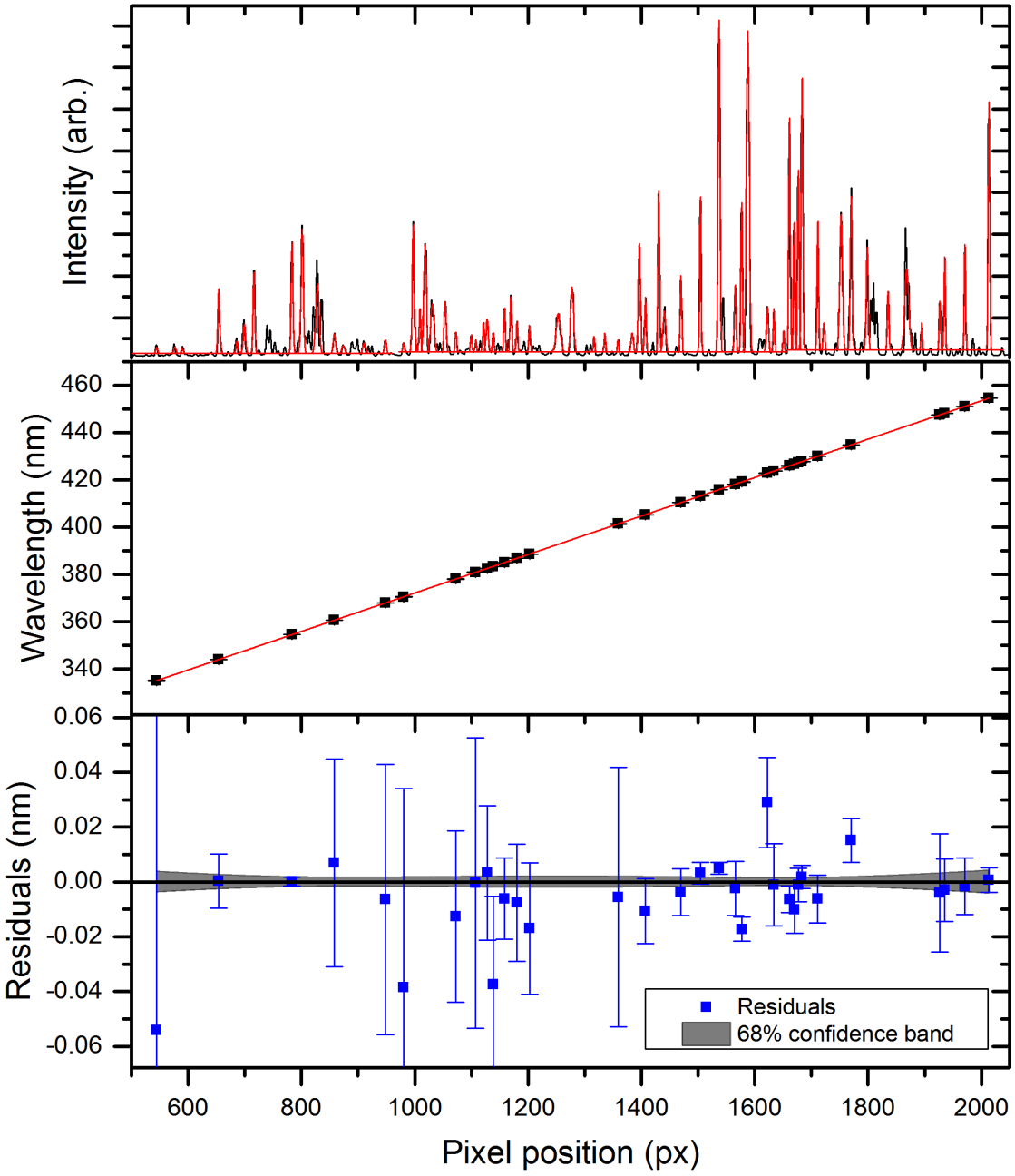

Figure 5.3: (top) The spectrum of the argon-iron lamp in the region of 290-470 nm with the applied Gaussian fits. (middle) The polynomial fit applied to the wavelengths of the reference lines plotted against the pixel positions of the peaks. (bottom) The residuals between the data points and the calibration function with the 68 % confidence band shown in gray.

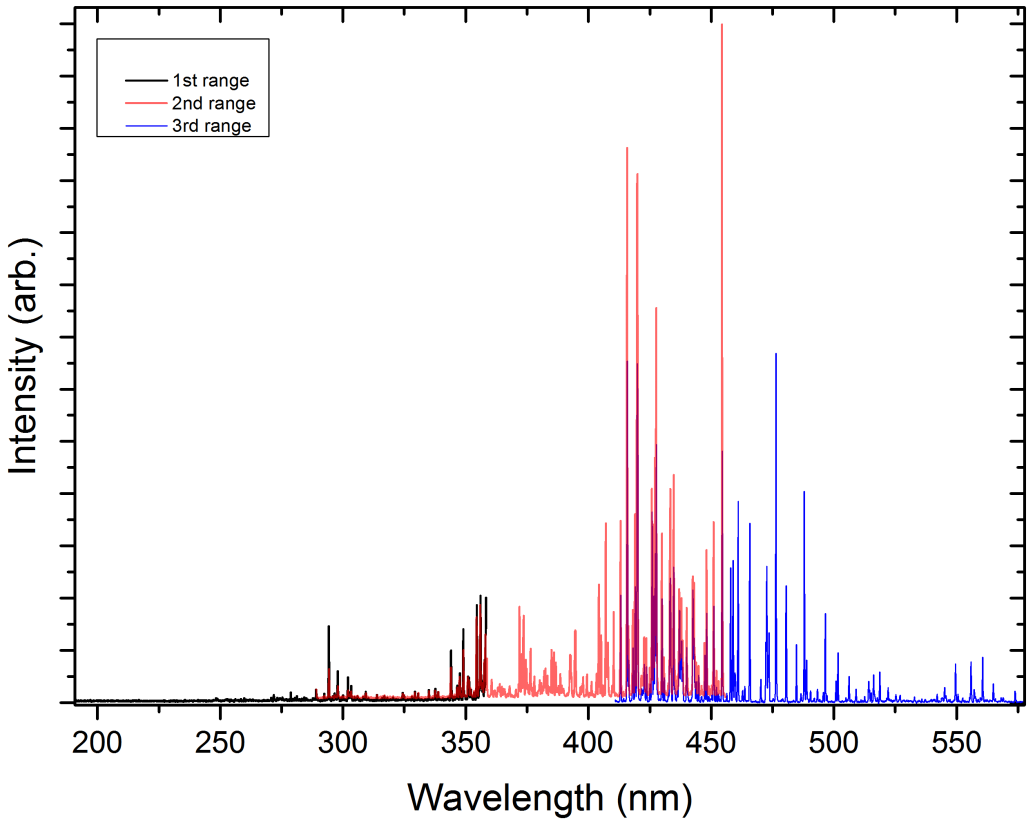

Figure 5.4: The spectrum of the argon-iron lamp composed of the three recorded calibration spectra for the different wavelength ranges. 1st range: 191-358 nm, 2nd range: 289-455 nm, 3rd range: 410-576 nm

areas, is shown in figure 5.4. For the overlap between the second and third wavelength region, the discrepancies among the calibration spectra are in the same order of magnitude as the width of the confidence band as can be seen in figure 5.5. However the discrepancies in the overlap between the first and second range are significantly higher, as the occurring deviation between the two calibration spectra yields up to 0.08 nm, as shown in figures 5.6 and 5.7. The recorded lines located in this overlap are therefore assigned with a calibration error calculated by determining the wavelength difference between a calibration line with a similar wavelength and the respective reference line.

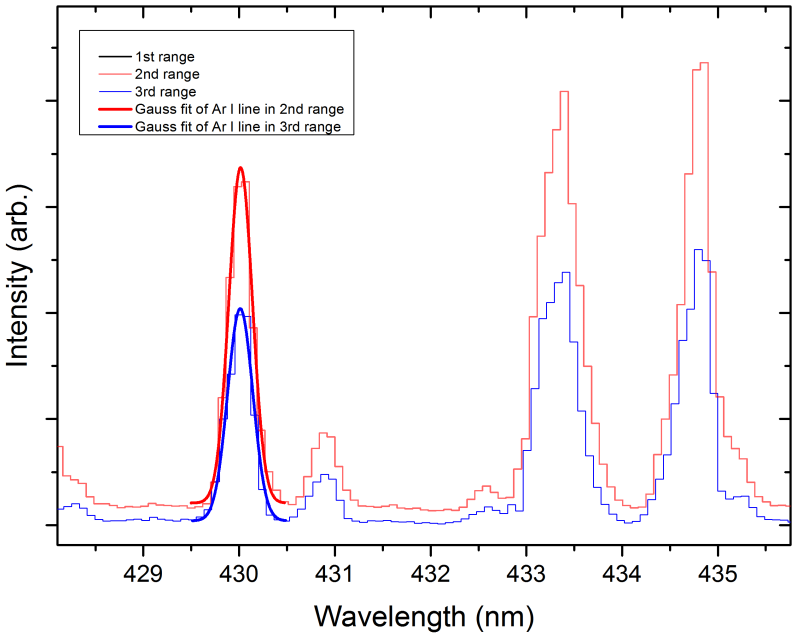

Figure 5.5: Close up of the overlap between the second and the third wavelength range. The distance from the reference line of Ar I (430.0101 nm) is 0.0064 nm for the second range and 0.0023 nm for the third range.

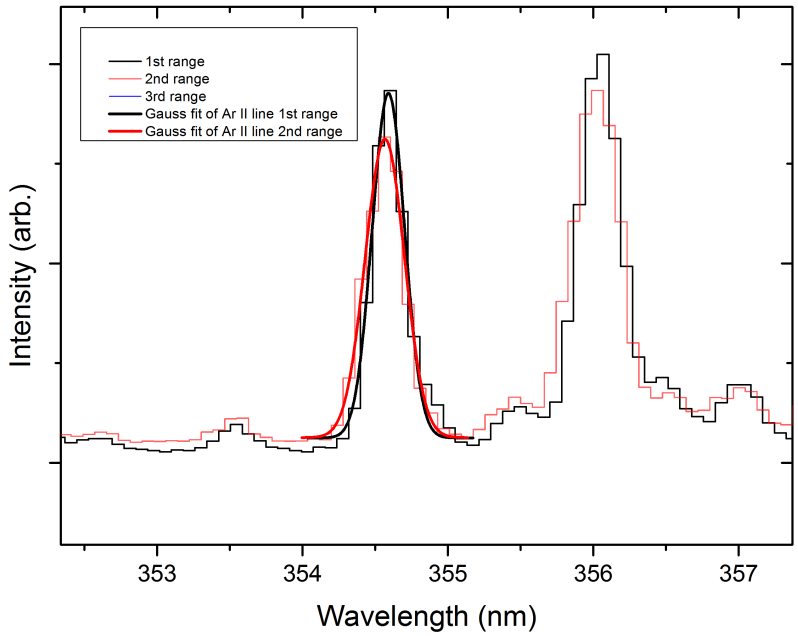

Figure 5.6: Close up of the right edge of the overlap between the first and the second wavelength range. The distance from the reference line of Ar II (354.58431 nm) is 0.0061 nm for the first range and 0.018 nm for the second range.

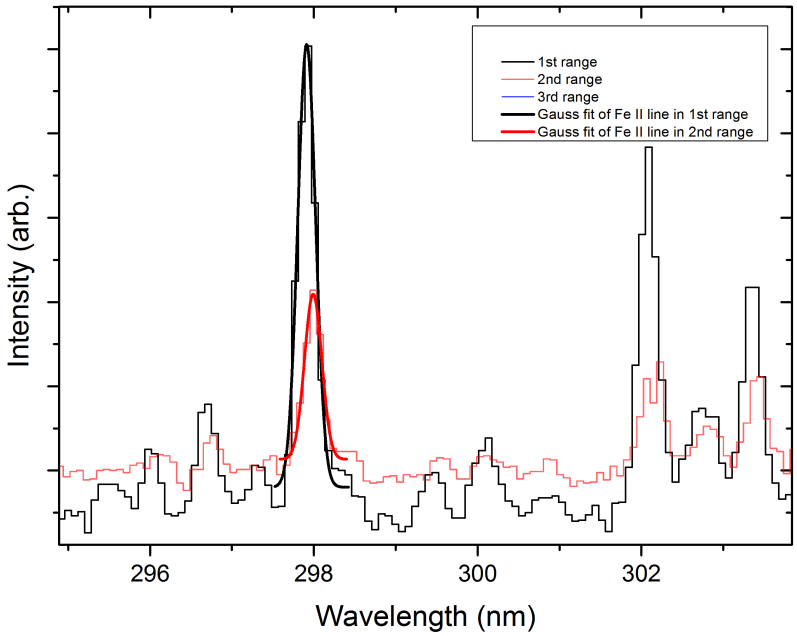

Figure 5.7: Close up of the left edge of the overlap between the first and the second wavelength range. The distance from the reference line of Fe II (297.9125 nm) is 0.001 nm for the first range and 0.080 nm for the second range.

5.4 Wavelength determination

The obtained spectra of the ion cloud first have to be corrected for the measured background. Since the background is obtained only once in the beginning of the measuring sequence, subtracting it does not account for small variations of the background over the time. Due to these fluctuations the arithmetical mean of the measured intensities of each bin is subtracted for every bin. The wavelength determination is not impaired by this as the background fluctuation affects the whole spectrum. The wavelengths of the spectral lines were obtained by fitting the peak in the spectrum where the maximum intensity of the line is reached with a Gaussian. The wavelength error is determined by combining the error of the Gaussian fit with the calibration error through error propagation.
To later be able to compare the lines with atomic theory calculations, the wavelengths are also converted to energies using

$$E = \frac{hc}{\lambda_{\mathrm{vac}}}. \tag{5.1}$$

with the Planck constant h and the speed of light c. The value of the product hc was taken from CODATA, $hc = 1239.841974(7)\,\mathrm{nm\,eV}$ [20]. The wavelengths were obtained with a spectrometer placed in air, therefore they have to be corrected with the refractive index of air n_{air} to obtain the wavelengths in vacuum needed for the conversion. This is performed as specified in [5] using

$$\lambda_{\mathrm{vac}} = n_{\mathrm{air}} \lambda_{\mathrm{air}} \tag{5.2}$$

$$n_{\mathrm{air}} = 1 + 10^{-8} \left(8342.13 + \frac{2406030}{130 - S^2} + \frac{15997}{38.9 - S^2} \right) \tag{5.3}$$

with $S = \frac{1000}{\lambda_{\mathrm{air}}}$. The lines are listed in table 5.1 with their respective charge state, their wavelength and their energy. After the determination of every line, the individual spectra of each energy scan are assembled resulting in a complete overview of the acquired data shown in figure 5.8 in dependence of the photon energy in electron volts.

Table 5.1: List of spectral lines of Ru^{9+} to Ru^{18+}. The wavelengths are given in λ_{air}. The errors set in bold face were calculated using the overlap error discussed in the previous section. The range indicates in which wavelength range the line was recorded. The ranges are 1: 191-358 nm, 2: 289-455 nm and 3: 410-576 nm

Charge State	Range	Wavelength (nm)	Energy (eV)	Label
9	1	302.716(8)	4.0945(1)	A
	2	302.7**(8)**	4.093(1)	A
10	1	336.504**(8)**	3.68342(9)	B
	2	336.51**(2)**	3.6834(2)	B
11	2	310.22**(8)**	3.995(1)	C
	1	310.167(4)	3.99618(7)	C
	3	427.46(1)	2.89962(9)	D
12	1	272.92(1)	4.5414(2)	E
	2	384.175(3)	3.22637(2)	F
	2	418.14(2)	2.9642(1)	G
	3	418.11(2)	2.96455(7)	G
	3	545.88(2)	2.27063(7)	H
13	1	254.656(7)	4.8672(1)	I
	1	254.698(6)	4.8664(1)	I
	3	487.96(2)	2.5402(1)	J
	3	509.455(4)	2.43298(2)	K
14	2	316.32**(2)**	3.9184(2)	L
	1	316.338**(9)**	3.9182(1)	L
	1	316.303**(6)**	3.91865(8)	L
	2	316.29**(2)**	3.9188(2)	L
15	1	269.529(7)	4.5987(1)	M
	1	297.577(7)	4.1652(1)	N
	2	346.43**(2)**	3.5779(2)	O
	1	346.415**(7)**	3.57804(7)	O
	2	366.474(5)	3.38220(5)	P
	3	436.55(2)	2.8393(1)	Q
	2	436.589**(8)**	2.83904(5)	Q
	3	436.511(6)	2.83955(4)	Q
	3	541.05(1)	2.29091(5)	R

??	2	336.99**(2)**	3.6782(2)	S
Charge State	Range	Wavelength (nm)	Energy (eV)	Label
??	1	336.948**(7)**	3.67856(5)	S
	2	422.56(1)	2.93330(7)	T
16	1	282.640(4)	4.38536(6)	U
	3	565.268(7)	2.19276(3)	V
17	2	297.52**(8)**	4.166(1)	W
	1	297.497(5)	4.16636(7)	W
	2	312.51**(2)**	3.9663(2)	X
	1	312.491(3)	3.96646(4)	X
	2	335.07**(2)**	3.6992(2)	Y
	1	335.058**(8)**	3.69932(9)	Y
	2	345.49**(2)**	3.5877(2)	Z
	1	345.474**(8)**	3.58779(9)	Z
	3	470.23(2)	2.6360(1)	α
18	2	326.97**(2)**	3.7907(3)	β
	1	326.99**(1)**	3.7905(1)	β
	2	332.52**(2)**	3.7275(2)	χ
	1	332.52**(1)**	3.7275(1)	χ
	1	342.644**(7)**	3.61741(7)	δ
	2	342.64**(2)**	3.6174(2)	δ
	2	378.22(1)	3.2772(1)	ϵ
	2	398.587(6)	3.10972(4)	ϕ
	3	416.92(2)	2.9729(1)	γ
	3	479.310(9)	2.58600(5)	η

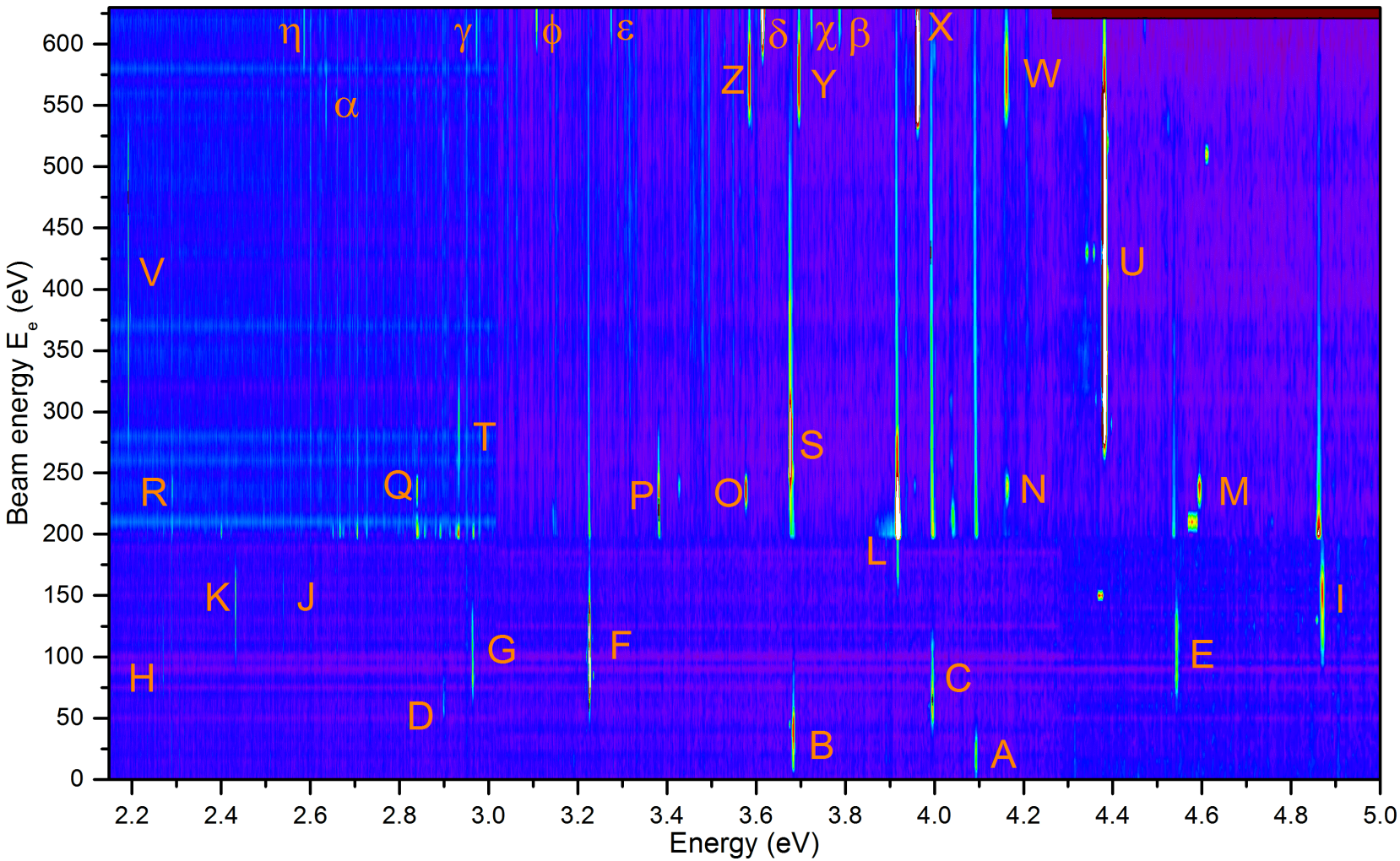

Figure 5.8: Composed color map of the six performed energy scans of ruthenium showing the charge states Ru^{9+} up to Ru^{18+}. The electron beam energy is given with an offset of 170 eV, the initial beam energy of the lower energy scans. The color scaling of the intensity is logarithmic to bring out the spectral lines with lower intensity. Every measured line is tagged with a letter, which is also listed in table 5.1.

5.5 Charge state determination

The assigned charge states displayed in table 5.1 have been determined with the help of theoretical calculations made by by J. Scofield [21], which are presented in table 5.2.Calculations performed with the flexible atomic code have later been made to further reinforce the assignment of the charge states. One of the obtained level schemes is shown exemplary for Ru^{13+} in figure 5.9, while the remaining ones are listed in the appendix. The first reference point for the charge state determination is the line U, which possesses a high intensity over an energy range of 300 eV. The only eligible charge state spanning over a similar energy range is Ru^{16+}, leading to the conclusion that line U is emitted by Ru^{16+}-ions. The other charge states are assigned based to this assumption, according to the energy differences ΔE of the respective states. Lines S and T remain the only ones that could not have been assigned to a charge state, since they are observed in between the charge states 15+ and 16+. Line T possibly originates from another ion that was temporarily present in the trap, since it could not have been measured consistently, appearing only in the third wavelength range but not in the second, as shown in figure 5.10. However line S is present in the first and second wavelength range, which cannot be explained with the current charge state determination.

Table 5.2: Ionization energies of the ions investigated in this work provided by calculations of J. Scofield. ΔE is the energy difference between the current and the following charge state.

Charge state	Ionization energy (eV)	ΔE (eV)
Ru^{9+}	178.5	21.6
Ru^{10+}	200.1	22.1
Ru^{11+}	222.2	26.6
Ru^{12+}	248.8	24.2
Ru^{13+}	273.0	23.9
Ru^{14+}	296.9	56.7
Ru^{15+}	353.6	26.1
Ru^{16+}	379.7	293.6
Ru^{17+}	673.3	57.8
Ru^{18+}	731.0	n.a.

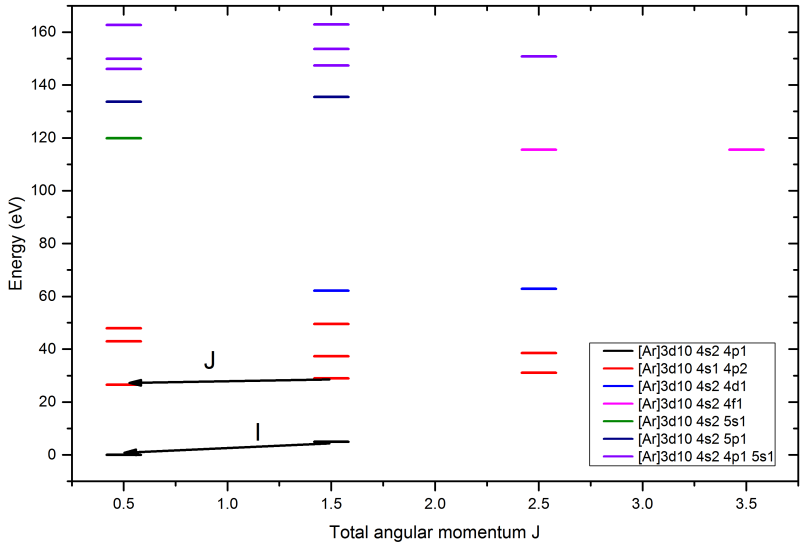

Figure 5.9: Grotrian level diagram of the energy levels of Ru^{13+} as calculated by FAC. The indicated level transitions are marked with the label of their respective line.

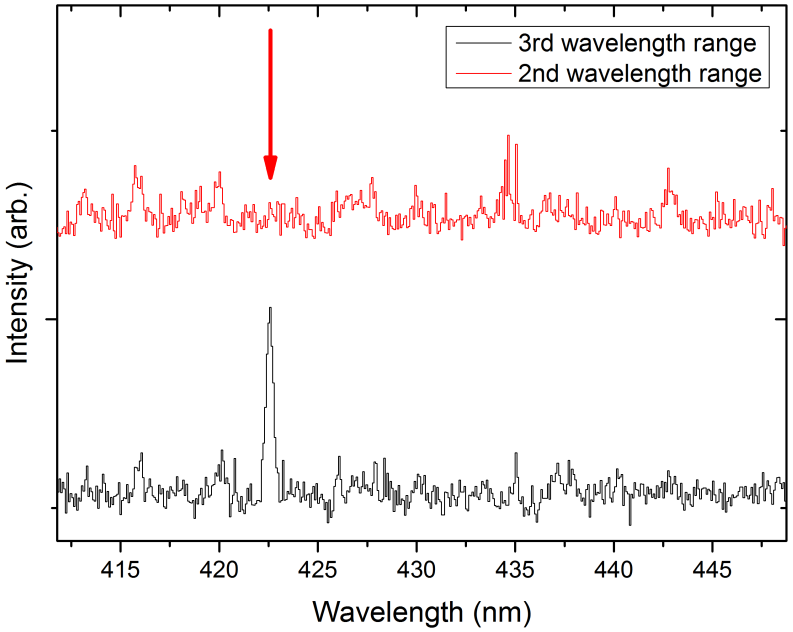

Figure 5.10: Comparison of the two spectra recorded in the ranges 2 (289-455 nm) and 3 (410-576 nm), showing that the line T is only appearing in the measurement of range 3.

To compare the theoretical calculations and the measured data, the intensity behavior of the individual charge states is plotted as a function of the electron beam energy E_e in figure 5.12. The lines corresponding to the 18+ charge state have a very low intensity, because the state is not yet satisfactory populated in the last measurement steps and are thus not included in this plot. The featured intensity profiles were obtained by adding all lines corresponding to the same charge state and normalizing the resulting profile. In order to combine the two different energy ranges of 170 eV to 400 eV and 520 eV to 900 eV they have to be corrected for their respective space charges. These are estimated to be 50 eV for the lower energy range and 180 eV for the higher energy range.

When examining the lower charge states 9+ to 12+, a shift of about 20 eV to a lower energies from the theoretical ionization energies is noticeable. This suggests an overestimated space charge potential for the lower energy range experiments, since the start of the intensity profiles should coincide with their respective calculated ionization energy. The intensity profile of the 12+ charge state first shows a steep increase of intensity, similar to the preceding charge states, but after reaching a maximum at 230 eV it declines over an energy range of 50 eV. An opposite behavior can be observed in the profile of the 13+ charge state, which shows a small increase of intensity over 50 eV before reaching the maximum at 310 eV and a very fast decline afterwards. The theoretical ionization energy is reflecting this early rise of intensity, since it is predicted for the charge states to have an energy difference of 24.2 eV, which still leaves the question why the maximum of the 13+ charge state intensity profile is only reached after approximately 60 eV. A possible explanation is the slow intensity decrease of the 12+ charge state, probably caused by a high number of Ru^{12+} ions still present in the trap. However, simulations of the charge state population distribution, performed with the private source program Dither, do not support this assumption, as can be seen in figure 5.11. The distribution is simulated for a beam energy of 295 eV using conditions similar to those of the experiment, resulting in the 13+ charge state representing 95% of the population. Thus no explanation can be given for the intensity profile shapes of the charge states 12+ and 13+.

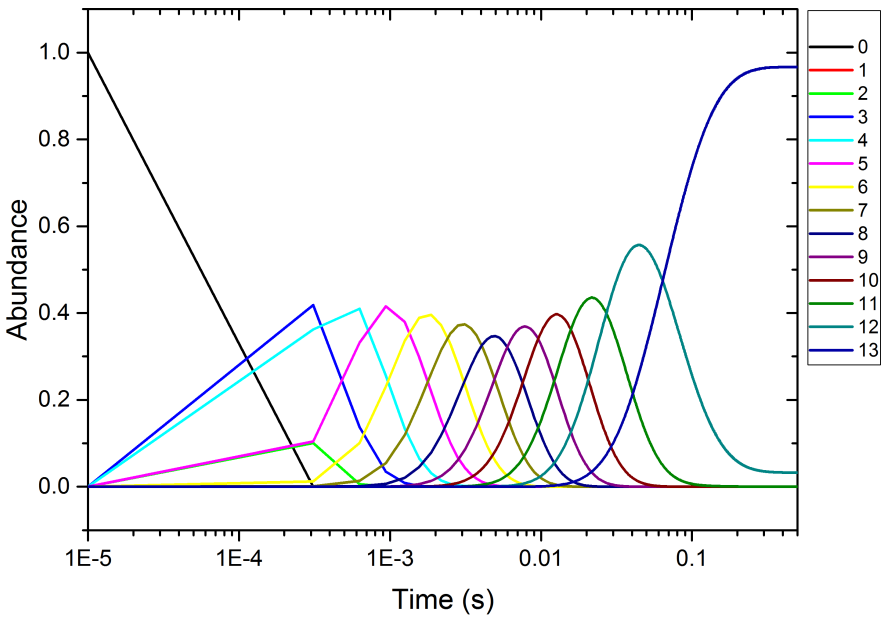

Figure 5.11: Simulation of the charge state population performed with dither for a 8 mA beam current and an electron beam energy of 295 eV. The time axis is displayed in a logarithmic scale.

The charge states 14+ to 17+ are in good agreement with the theoretical calculations as their intensity profiles all coincide with the respective ionization energies, with the exception of 16+. Here the predicted ionization energy is approximately 30eV lower than the start of the intensity profile. The shift results in an agreement between the start of the intensity profile of the unknown charge state related to the line S and the ionization energy of the 16+ charge state. This may be a hint for the origin of this line which will be further discussed in the following section.

The intensity profile of the 15+ charge state is the only one that is represented by a very narrow peak. This is due to lines Q, O, N and M that are only visible for a small energy range of 30 eV, in contrast to the lines of other charge states which are prominent for a range of about 60 eV. Only the line P of the 15+ charge state has an intensity profile similar to the ones of other charge states. However, so far no explanation can be given for this unique behavior.

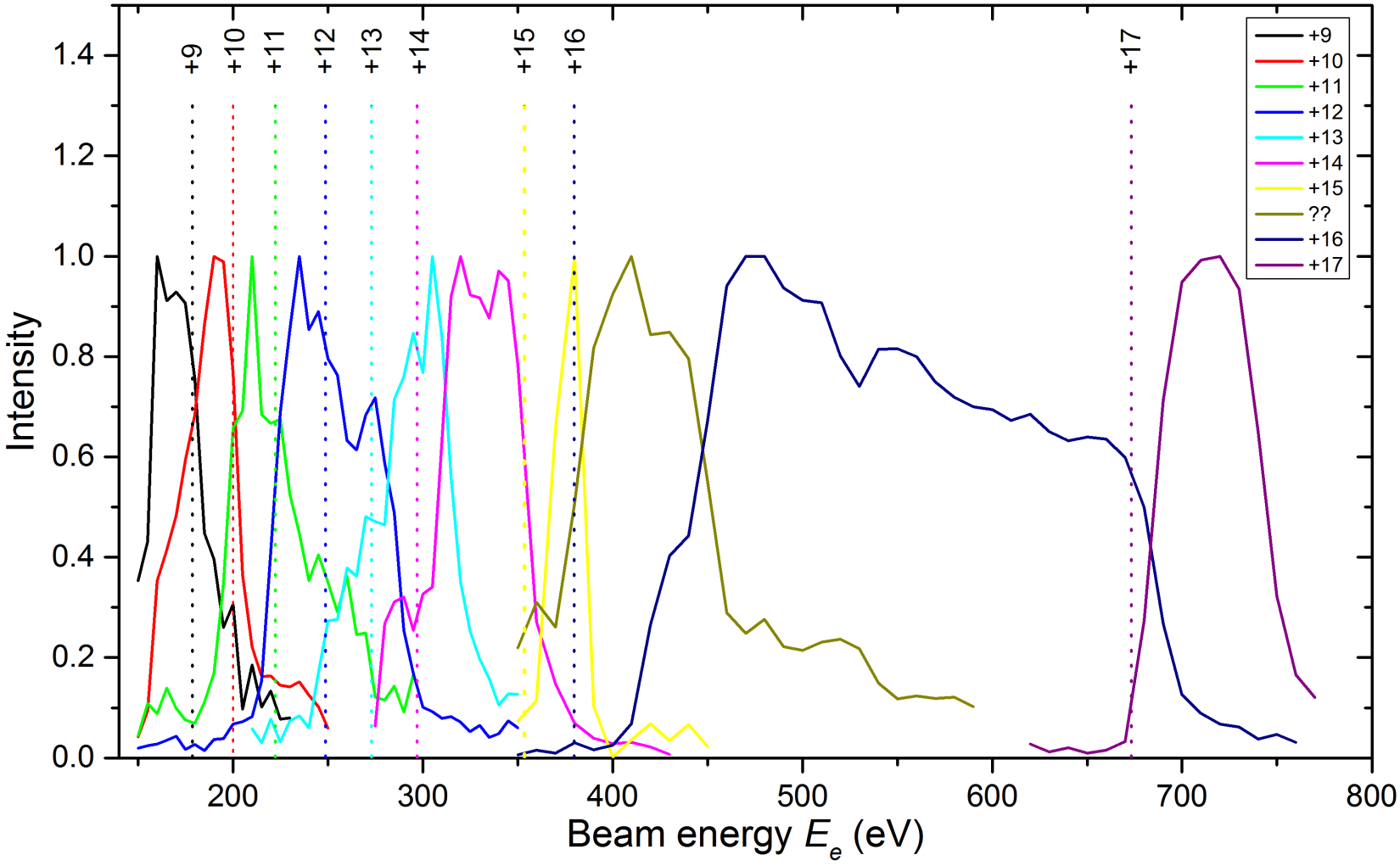

Figure 5.12: Intensity behavior of the ruthenium lines as a function of the electron beam energy. The beam energy is corrected for the occurring space charge potential, refer to the main text for more details. The ionization energies are displayed with the vertical dashed lines.

5.6 Comparison to atomic theory

The FAC calculations, addressed in the previous chapter, have been performed for every charge state of ruthenium investigated in this work. As there is no other theoretical data available, these calculations are the only reference for the determination of the observed transitions.

First, the energy levels and the transition probabilities between the said levels were calculated. The code used for this calculations had to be adjusted for each individual charge state. The electron shells below the first not completely filled shell are considered as closed shells, meaning that electronic excitations from these shells are not included in the calculation. This includes the shells $1s$, $2s$, $2p$, $3s$ and $3p$ for every calculation, $3d$ for the calculations below the 15+ charge state and $4s$ for the charge states below 14+. The shells that were included in the individual calculations are displayed in the respective Grotrian diagrams in the appendix. Performing these calculations supplied all the possible electronic configurations and their energies in regards to the included electron shells. Because of the numerous configurations and the even higher number of possible transitions between them, the measured transitions cannot be identified with a satisfactory certainty. Therefore a collisional radiative modeling (CRM) has been made to include the electron impact excitation, and de-excitation processes occurring in the EBIT.

In this model, the electron beam properties present for the individual charge state measurements had to be included, which have been taken from previous simulations made by H. Bekker [5], with exception of the electron beam density, which was set to $10^{11}\,\mathrm{cm}^{-3}$, and the electron beam energy, which was set to an energy 20 eV higher than the ionization energy of the respective charge state. The rate equations were solved with these settings and a synthetic spectrum was created for each charge state in the investigated photon energy range. The result is shown in figure 5.13, presenting the modeled color map similar to figure 5.8, obtained through combining the created spectra.

Using these calculations, most of the measured lines could have been assigned to an intra configuration transition, which energies are displayed together with the measured photon energies of the corresponding line in table 5.3. Each transition is visualized in the Grotrian diagrams, with an arrow starting from the upper energy level and pointing to the lower level of the transition. The label of each measured line is also used to label the corresponding calculated transition in the Grotrian diagrams as well as the synthetic spectrum.

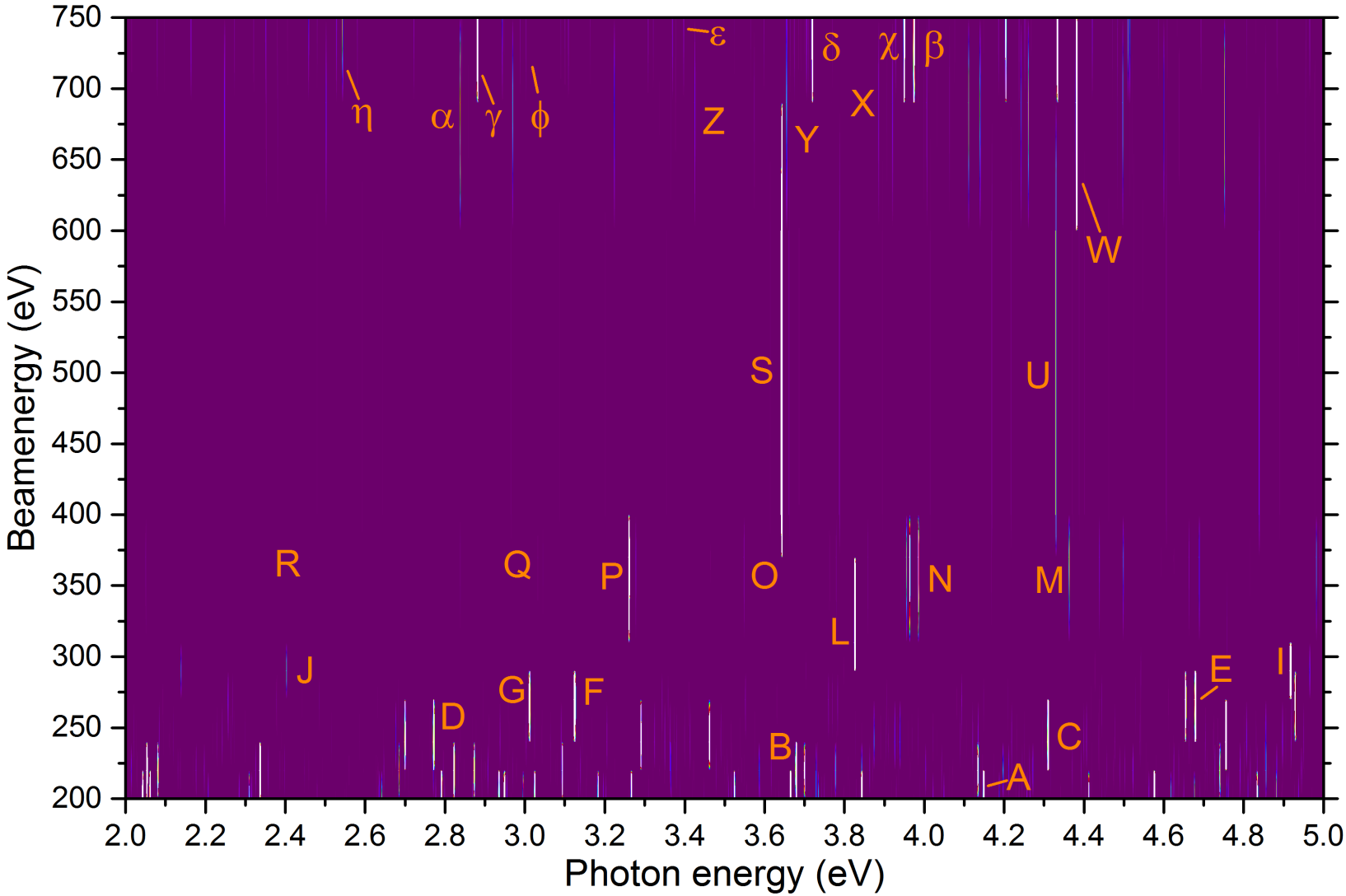

Figure 5.13: Color map of the synthetic spectrum of Ru^{9+} to Ru^{18+}. The spectrum was obtained with the CRM model.

Table 5.3: List of spectral lines of Ru^{9+} to Ru^{18+} together with their transition energy as calculated with FAC. Values of lines that were recorded multiple times were obtained by calculating the weighted mean of these lines.

Label	Charge state	Measured energy	FAC calculation (eV)
A	9	4.094(1)	4.148844
B	10	3.6834(8)	3.679477
C	11	3.9961(9)	4.309919
D	11	2.89962(9)	2.771703
E	12	4.5414(2)	4.679065
F	12	3.22637(2)	3.125138
G	12	2.9644(6)	3.012064
H	12	2.27063(7)	2nd order of E
I	13	4.867(1)	4.917998
J	13	2.5402(1)	2.403241
K	13	2.43298(2)	2nd order of I
L	14	3.9185(6)	3.826422
M	15	4.5987(1)	4.363037
N	15	4.1652(1)	3.985569
O	15	3.5780(7)	3.548676
P	15	3.38220(5)	3.261143
Q	15	2.8393(4)	3.045619
R	15	2.29091(5)	2.460174
S	16	3.6785(6)	3.643454
T	-	2.93330(7)	-
U	16	4.38536(6)	4.329961
V	16	2.19276(3)	2nd Order of U
W	17	4.167(1)	4.381599
X	17	3.9664(7)	3.885674
Y	17	3.6993(8)	3.655596
Z	17	3.5878(8)	3.425308
α	17	2.6360(1)	2.838258
β	18	3.791(1)	3.974222
χ	18	3.7275(9)	3.9498423
δ	18	3.6174(7)	3.719746
ϵ	18	3.2772(1)	3.397970

ϕ	18	3.10972(4)	3.002810
γ	18	2.9729(1)	2.881759
η	18	2.58600(5)	2.543725

The lines obtained from the lower charge states of ruthenium up to Ru^{14+} (A-L) are corresponding to strong transitions in the ground state configuration, which are all in agreement with the theoretical values within a range of ± 0.1 eV, except for the line C, which has deviation of -0.3 eV from the theoretical prediction. A reason for this high discrepancy might be the calibration, as line is recorded in the overlap region where the overlapping calibration spectra have a high deviation. The only lines not originating from a transition in the ground state are the lines G, J and L. However they originate from the configurations which are the energetically closest to their respective ground states. The lines A to L are also the ones with the highest intensities in the simulated spectra, as can be seen in figure 5.13. Nevertheless the CRM model predicts more optical transitions in these charge states, which do not appear in the measurement data. Line H, has the same behavior as line E while having a much lower intensity. As the photon energy of this line is exactly half the photon energy of the line E, it is concluded that line H is the second diffraction order of line E. Following this reasoning, the lines K and V are also identified as second diffraction orders of the lines I and U, respectively.

The electronic configurations of the higher charge states are much more complex, due to the fact that the $3d$ shell, containing up to 10 electrons is no longer considered as a closed shell. This affects the calculation of the transition energies, leading to overall higher discrepancies between the theoretical calculations and the experimental data. However the calculated transitions corresponding to the measured lines are still among the ones with the highest transition rate in the CRM model. Four of the observed transitions of Ru^{15+} (O, P, Q and R) occur in the $3d^9 4s^1 4p^1$ configuration, while the line M represents a transition in the $3d^9 4s^2$ configuration. The remaining line N is the only one that is represented by an inter shell transition between $6g^1$ and $6f^1$. The 15+ charge state thus features no measured optical transitions near the ground state, in contrast to the other charge states investigated in this work. The Grotrian diagram of Ru^{15+} is given in figure 5.14 and a close up of the diagram in figure 5.15.

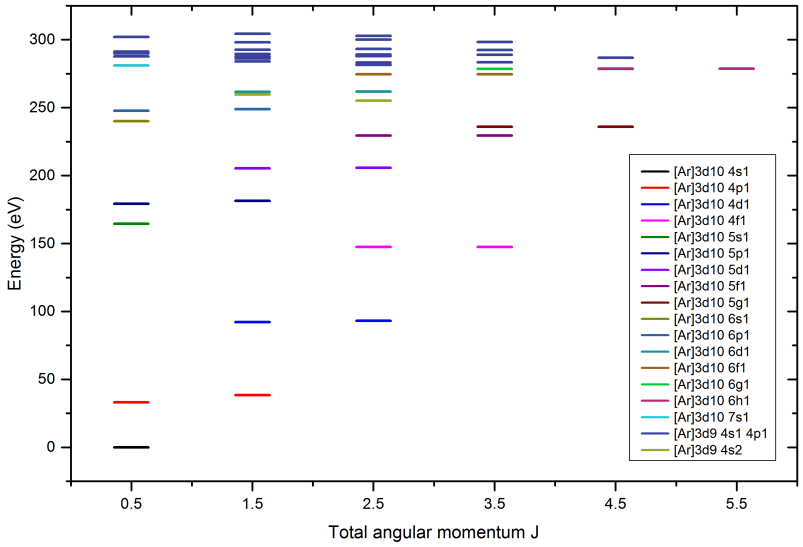

Figure 5.14: Grotrian level diagram of the energy levels of Ru^{15+} as calculated by FAC. The occurring transitions are featured in the following close up.

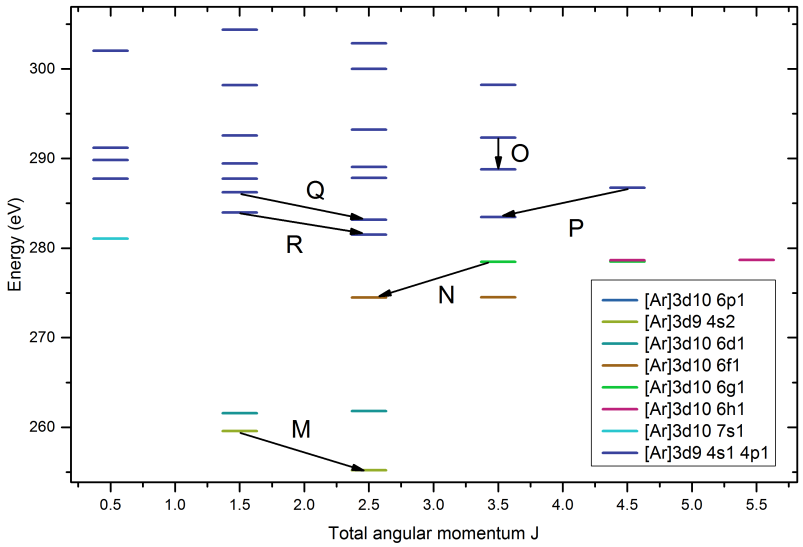

Figure 5.15: Close up Grotrian level diagram of the energy levels of Ru^{15+} as calculated by FAC. The indicated level transitions are marked with the label of their respective line.

The lines obtained from the charge states Ru^{16+} to Ru^{18+} all correspond to transi-

tions in the ground state configurations and the configurations energetically closest to the ground state.

Only two strong transitions are visible in the synthetic spectrum of Ru^{16+}, whereat U corresponds to the lowest possible optical transition in the $3d^9 4s^1$ configuration. However the stronger of the two visible transitions energetically corresponds to the line S, which has no assigned charge state. As already mentioned, the ionization energy for the 16+ charge state matches with the intensity profile of the line S. Additionally, the line is in good agreement with the theoretical calculation, which leads to the assumption that line S originates from Ru^{16+}-ions. But under consideration of the significant difference in the beam energy dependence of the two lines S and T it becomes apparent that these lines cannot belong to the same charge state.

The intensities of the lines that were recorded in the 17+ charge state feature a deviation from the theoretical calculations. Line W is the second weakest of the recorded Ru^{17+} transitions whereas the corresponding calculated line is the brightest in the synthetic spectrum of Ru^{17+}. Additionally, the brightest line in the recorded spectrum (line X) is among the transitions with the lowest intensities in the synthetic spectrum. Line W is assumed to be the brightest line, as it is corresponding to the single possible transition in the ground state configuration $3d^9$, while the remaining transitions occur in the $3d^8 4s^1$ configuration. However, this line features also a comparatively high energy deviation of -0.21 eV from the theoretical value, which could indicate that the energy of the intra ground state transition is overestimated in the calculation.

Due to the limited energy range of the recorded spectra, the lines originating from Ru^{18+}-ions do not reach their maximum intensities. As a result, the accuracy of the wavelength determination is reduced and their intensities cannot be compared with the lines of the synthetic spectrum. A total of seven transitions have been recorded, three in the $3d^8$ ground state configuration and four in the $3d^7 4s^1$ configuration. Ru^{18+} is thus the charge state with the highest number of transitions recorded in this experiment, making it an interesting subject for future measurements in addition to the determination of the origin of the line S.

6 Summary and outlook

The investigation of ruthenium ions in the charge states Ru^{9+} to Ru^{18+} that has been performed at the HD-EBIT, resulted in a first set of 30 identified transitions in the wavelength range of 220-576 nm, which is shown in the table 6.1. The transition energies have been compared to atomic theory, using FAC calculations that were also performed in this work. The discrepancies between the measurements and theoretical calculations are within a reasonable range, considering the complexity of the calculations due to a high number of electrons included in the model.

Two more lines, S and T, have been measured with wavelengths of $\lambda_S = 336.96(6)$ nm and $\lambda_T = 422.56(1)$ nm, but could not be identified. The Line T presumably originates from a contaminant temporarily residing in the trap, since it was not measured consistently. Line S appears to belong to an intra configuration transition occurring in the $3d^9 4s^1$ configuration of R^{16+}. However, the electron beam energy dependency of this line agrees with neither the calculated ionization energies, nor the other recorded line of the Ru^{16+} charge state. Therefore the identification of this line remains a challenge for future measurements.

Another objective of future investigations is to confirm the identified transitions with other identification methods. One approach is to compare the measurements to other theoretical models besides FAC, for example the multi-configuration Dirac-Fock code (MCDF) [22]. Also, investigations of the individual line shapes can be performed by observing the Zeeman splitting of these lines and comparing them to theoretical line shape predictions made for each transition.

Additionally, in order to further complete this data set, measurements with low electron beam energies should be performed to investigate the lower charge states of ruthenium.

As mentioned in the introduction, spectral data of technetium is needed to forward the investigations of the white dwarf RE 0503-289. To accomplish this task a vacuum ultra violet spectrometer has been developed recently and is currently being tested. Also it is planned to design a new injection system that satisfies the requirements given by the radioactive nature of technetium.

Table 6.1: Transitions of Ru^{9+} to Ru^{18+} identified in this work, with their energies as calculated with FAC.

Charge state	Measurement (eV)	FAC calculation (eV)	Difference (eV)
9	4.094(1)	4.149	-0.055
10	3.6834(8)	3.6795	+0.0039
11	3.9961(9)	4.3099	-0.3138
	2.89962(9)	2.7717	+0.12792
12	4.5414(2)	4.6791	-0.1377
	3.22637(2)	3.12514	+0.10123
	2.9644(6)	3.0121	-0.0477
13	4.867(1)	4.918	-0.051
	2.5402(1)	2.403241	+0.137
14	3.9185(6)	3.8264	+0.0921
15	4.5987(1)	4.3630	+0.2357
	4.1652(1)	3.9856	+0.1796
	3.5780(7)	3.549	+0.029
	3.38220(5)	3.26114	+0.12110
	2.8393(4)	3.0456	-0.2063
	2.29091(5)	2.46017	-0.16926
16	4.38536(6)	4.32996	+0.0554
17	4.167(1)	4.382	-0.215
	3.9664(7)	3.8857	+0.0807
	3.6993(8)	3.6556	+0.0437
	3.5878(8)	3.4253	+0.1625
	2.6360(1)	2.838	-0.202
18	3.791(1)	3.974	-0.183
	3.7275(9)	3.9498	-0.2223
	3.6174(7)	3.7197	-0.1023
	3.2772(1)	3.398	-0.1208
	3.10972(4)	3.00281	+0.10691
	2.9729(1)	2.8818	+0.0911
	2.58600(5)	2.544	+0.042

7 Appendix

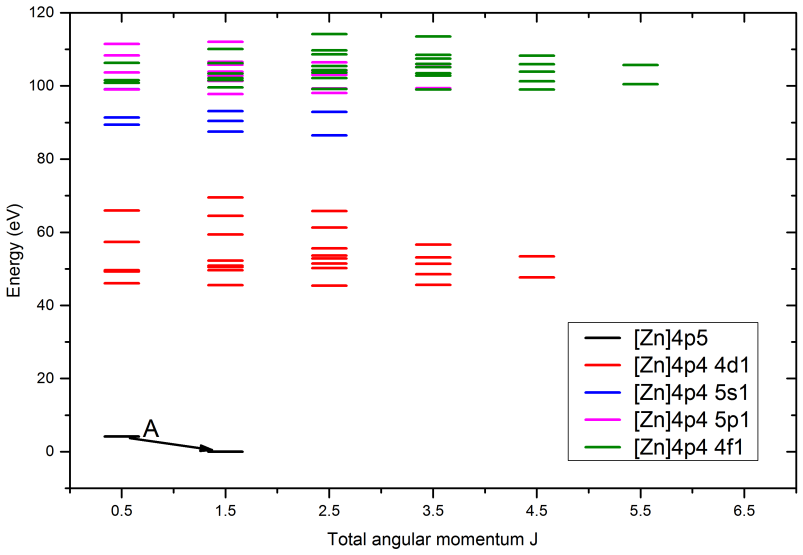

Figure 7.1: Grotrian level diagram of the energy levels of Ru^{9+} as calculated by FAC. The indicated level transition is marked with the label of the respective line A.

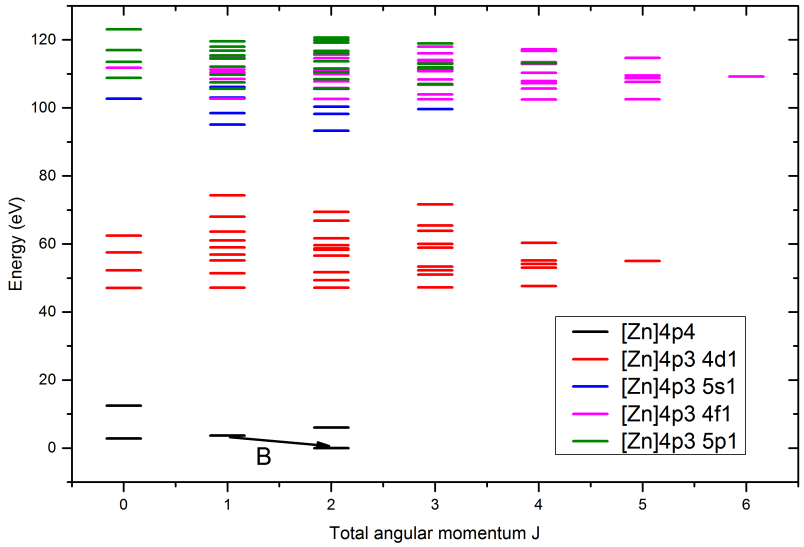

Figure 7.2: Grotrian level diagram of the energy levels of Ru^{10+} as calculated by FAC. The indicated level transition is marked with the label of the respective line B.

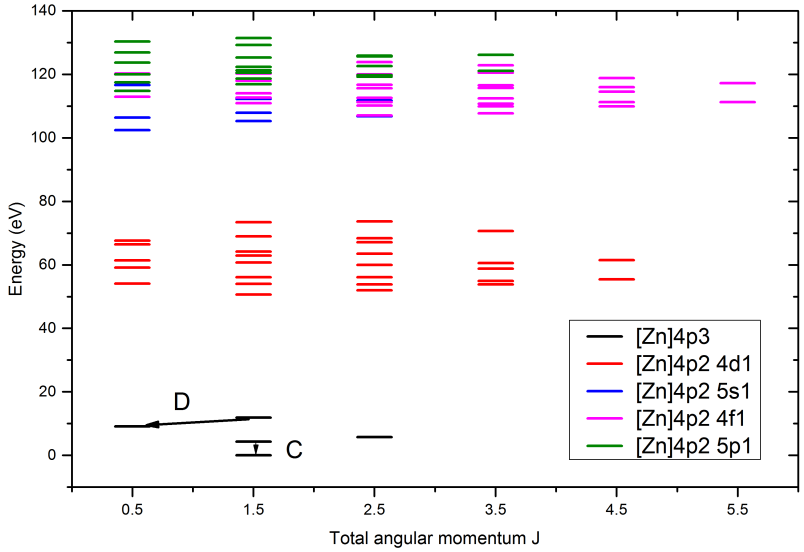

Figure 7.3: Grotrian level diagram of the energy levels of Ru^{11+} as calculated by FAC. The indicated level transitions are marked with the label of their respective line.

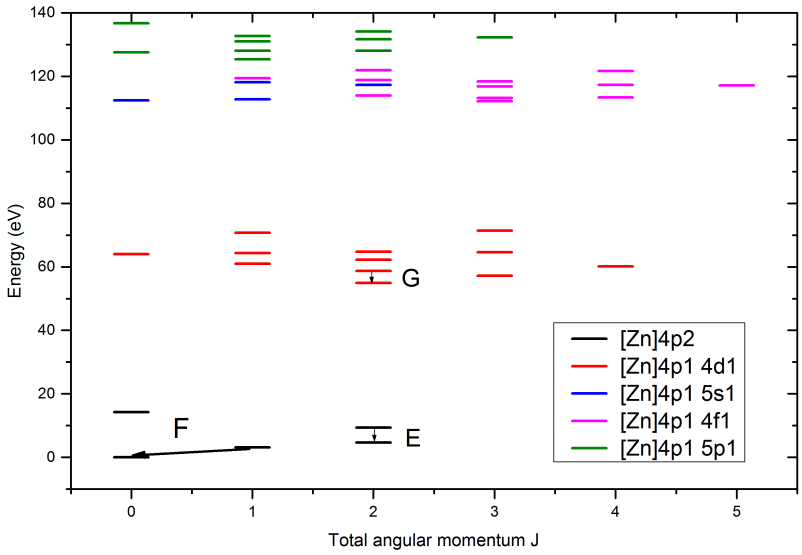

Figure 7.4: Grotrian level diagram of the energy levels of Ru^{12+} as calculated by FAC. The indicated level transitions are marked with the label of their respective line.

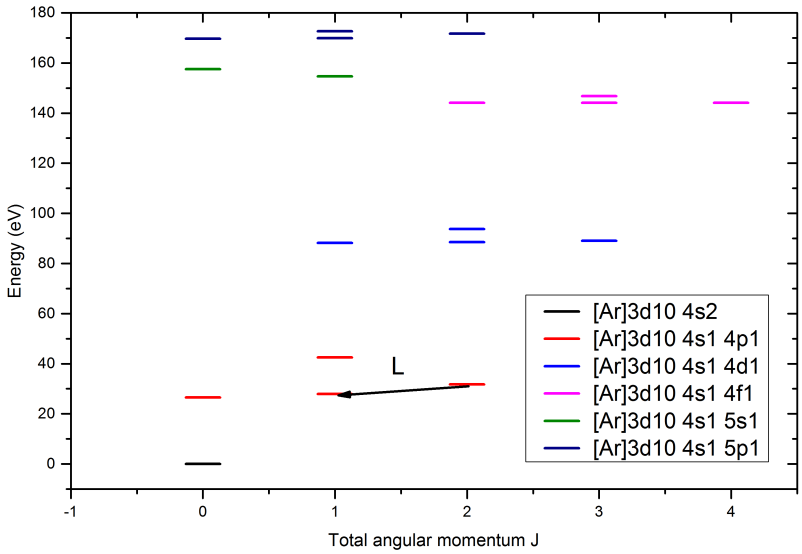

Figure 7.5: Grotrian level diagram of the energy levels of Ru^{14+} as calculated by FAC. The indicated level transition is marked with the label of the respective line L.

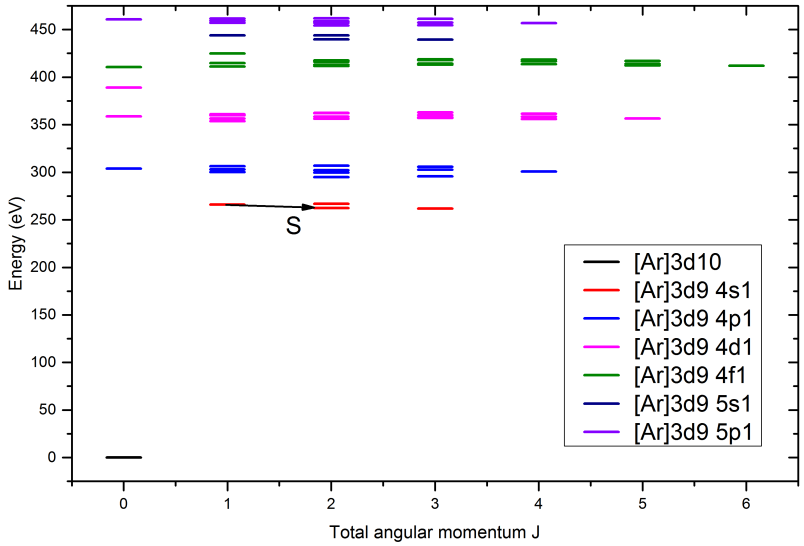

Figure 7.6: Grotrian level diagram of the energy levels of Ru^{16+} as calculated by FAC. The indicated level transition is marked with the label of the respective line S, other occurring transitions are featured in the following close up.

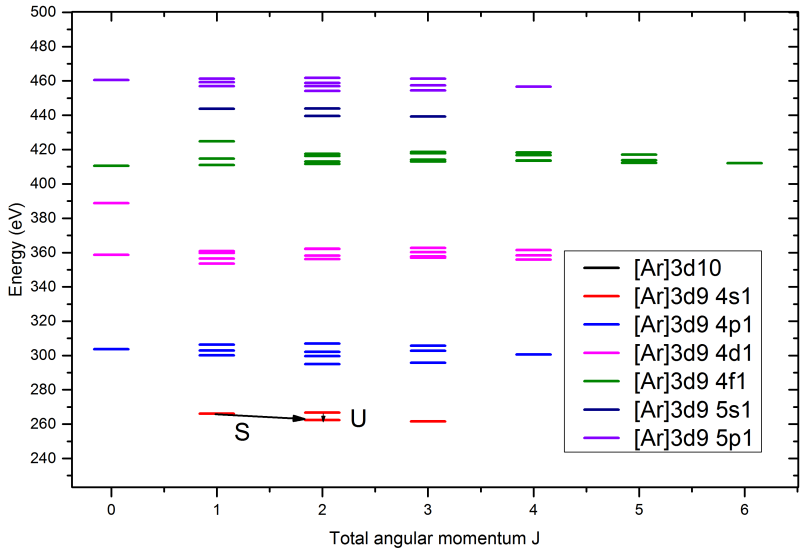

Figure 7.7: Close up Grotrian level diagram of the energy levels of Ru^{16+} as calculated by FAC. The indicated level transitions are marked with the label of their respective line.

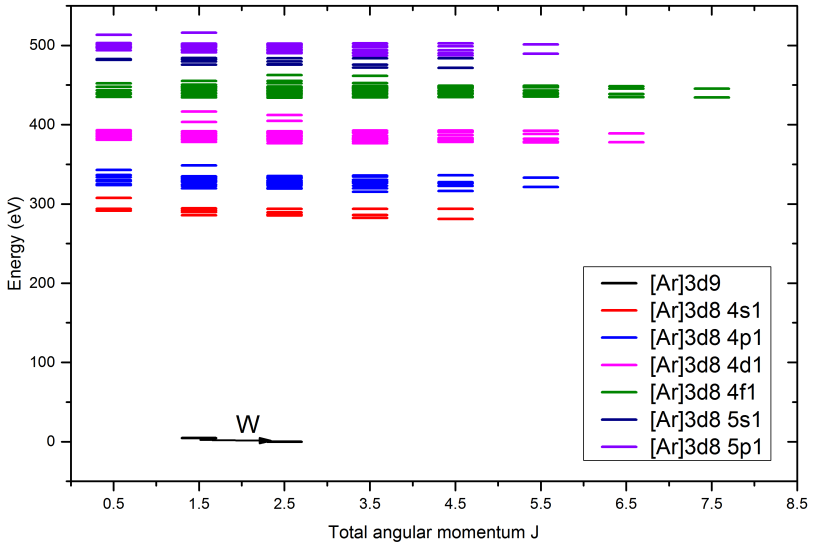

Figure 7.8: Grotrian level diagram of the energy levels of Ru^{17+} as calculated by FAC. The indicated level transition is marked with the label of the respective line W, other occurring transitions are featured in the following close up.

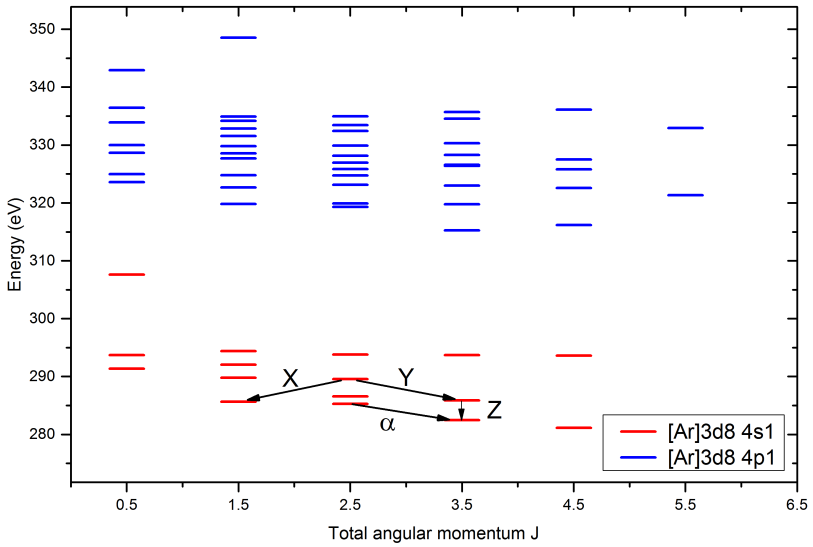

Figure 7.9: Close up Grotrian level diagram of the energy levels of Ru^{17+} as calculated by FAC. The indicated level transitions are marked with the label of their respective line.

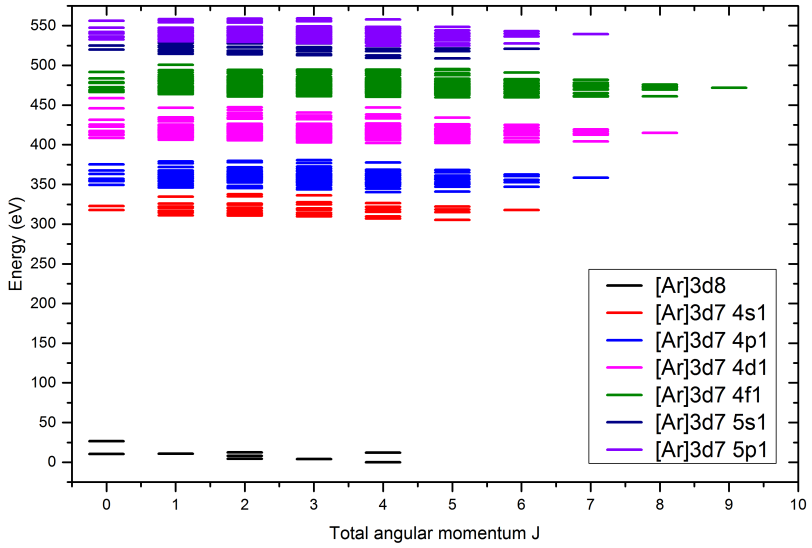

Figure 7.10: Grotrian level diagram of the energy levels of Ru^{18+} as calculated by FAC. The occurring transitions are featured in the two following close ups.

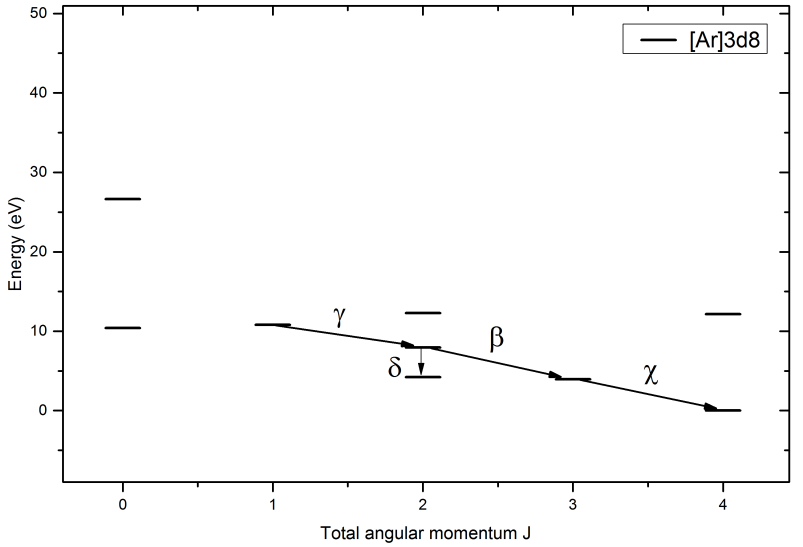

Figure 7.11: Close up Grotrian level diagram of the energy levels of Ru^{18+} as calculated by FAC. The indicated level transitions are marked with the label of their respective line.

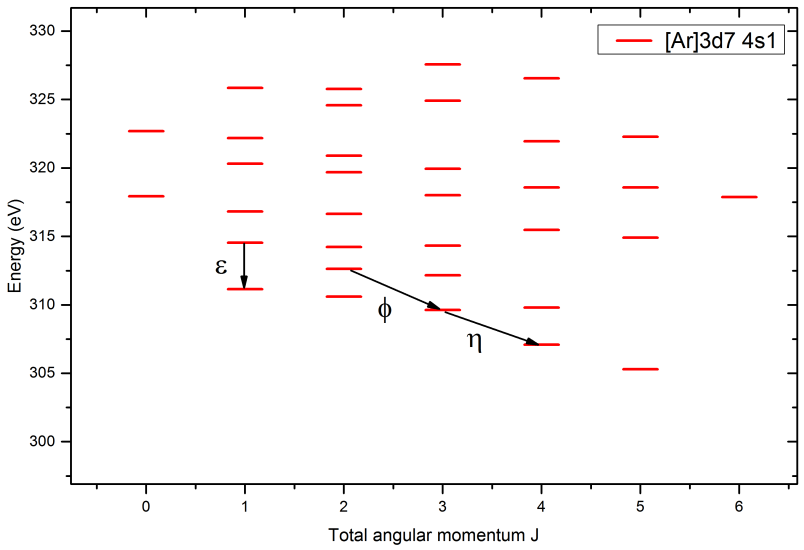

Figure 7.12: Close up Grotrian level diagram of the energy levels of Ru^{18+} as calculated by FAC. The indicated level transitions are marked with the label of their respective line.

Bibliography

[1] E. Ringat K. Werner, T. Rauch and J. W. Kruk. First Detection of Krypton and Xenon in a White Dwarf. *The Astrophysical Journal Letters*, 753, 2012.

[2] P. W. Merrill. Spectroscopic Observations of Stars of Class S. *Astrophysical Journal*, 116, 1952.

[3] S. Kucas K. Werner, T. Rauch and J. W. Kruk. The prospective search for highly ionized technetium in hot (pre-) white dwarfs. *Astronomy Astrophysics*, 574, 2015.

[4] J. Reader A. Kramida, Yu. Ralchenko and NIST ASD Team. NIST Atomic Spectra Database. *Available at http://physics.nist.gov/asd*, 2016.

[5] H. Bekker. Optical and EUV spectroscopy of highly charged ions near the $4f$-$5s$ level crossing. Dissertation, Ruprecht-Karls-Universität, Heidelberg, 2016.

[6] T. Mayer-Kuckuk. *Atomphysik - Eine Einführung*. B. G. Teubner, Stuttgart, 4. edition, 1994.

[7] W. Demtröder. *Experimentalphysik 3 - Atome, Moleküle und Festkörper*. Springer-Verlag, Berlin Heidelberg New York, 5. edition, 2016.

[8] M. F. Gu. The flexible atomic code. *Canadian Journal of Physics*, 86, 2008.

[9] H. K. Chung. *The How To For FLYCHK*. NIST, 2008.

[10] S. Bernitt. Resonante anregung astrophysikalischer röntgen-übergänge in hochgeladenen eisenionen mit dem freie-elektronen-laser LCLS. Dissertation, Ruprecht-Karls-Universität, Heidelberg, 2013.

[11] A. J. González Martínez. Quantum interference in the dielectronic recombination of heavy highly charged ions. Dissertation, Ruprecht-Karls-Universität, Heidelberg, 2005.

[12] G. Herrmann. Optical theory of thermal velocity effects in cylindrical electron beams. *Journal of Applied Physics*, 29, 1958.

[13] A. Windberger et al. Identification of the Predicted $5s$-$4f$ Level Crossing Optical Lines with Applications to Metrology and Searches for the Variation of Fundamental Constants. *Phys. Rev. Lett.*, 114, 2015.

[14] M. A. Blessenohl. Optische spektroskopie an hochgeladenen bismut-ionen und konstruktion eines hochauflösenden VUV-gitterspektrometers. Master's thesis, Ruprecht-Karls-Universität, Heidelberg, 2015.

[15] E. Hecht. *Optics*. Pearson, München, 4. edition, 2014.

[16] R. Klawitter. Resonant laser spectroscopy of a visible dipole transition in Ar^{+13}. Diploma thesis, Ruprecht-Karls-Universität, Heidelberg, 2009.

[17] W. Pych. A Fast Algorithm for Cosmic-Ray Removal from Single Images. *Publications of the Astronomical Society of the Pacific*, 116, 2003.

[18] A. Windberger. Identification of optical transisitons in complex highly charged ions for applications in meterology and tests of fundamental constants. Dissertation, Ruprecht-Karls-Universität, Heidelberg, 2015.

[19] N. Potters. Spektroskopische Untersuchung der optischen übergänge von den hochgeladenen Praseodym-ionen Pr^{9+} bis Pr^{13+}. Bachelor thesis, Ruprecht-Karls-Universität, Heidelberg, 2016.

[20] D. B. Newell P. J. Mohr and B. N. Taylor. Codata recommended values of the fundamental physical constants: 2014. *Rev. Mod. Phys.*, 88, 2016.

[21] J. Scofield. Ionization Energies. *LLNL Internal Report*, 1975.

[22] P. L. Hagelstein and R. K. Jung. Relativistic Distorted-Wave Calculations of Electron Collision Cross Sections and Rate Coefficients for Ne-like Ions. *Atomic Data and Nuclear Data Tables*, 37, 1987.

Acknowledgments

Als Erstes möchte ich dem gesamten EBIT-Team danken. Natürlich in erster Linie für die Unterstützung und die vielen Ratschläge, die ich im Laufe der Zeit am Institut von euch erhalten habe. Aber auch für die vielen Stunden, die über die Arbeit am MPIK hinaus gingen, seien es Abende in der Heidelberger Altstadt, die DPG Tagung in Mainz, oder einfach die lebhaften Gespräche am Kaffeetisch jeden Mittag. Ohne euch wär mein Einstieg in die Experimentalphysik mit Sicherheit nur halb so schön gewesen.

Ein besonderer Dank gilt Hendrik Bekker für seine kompetente Einweisung in die Handhabung der Heidelberg-EBIT, seine Bereitschaft mir über Messenger Apps, auch außerhalb seiner Arbeitszeit, jede mögliche Physik-Frage zu beantworten und für seine Hilfe bezüglich des Verfassens und der Korrektur dieser Arbeit.

Außerdem möchte ich José für seine aufmunternden Worte gegen Ende meiner Bachelorarbeit danken und auch dafür, dass ich die Chance bekommen habe diese am MPIK zu schreiben.

Weiterhin möchte ich mich bei allen Freunden bedanken, die ich in meiner bisherigen Zeit in Heidelberg kennen gelernt habe. Ohne euch hätte ich es sicher nicht so weit gebracht! Besonders möchte ich noch Freerik Forndran und Alexander Bigalke für die Korrektur dieser Arbeit danken.

Schließlich danke ich noch meiner Familie, die mich in meinem Studium unterstützt, auch wenn ich nicht immer viel Zeit für sie habe und Gladys Gress, die mich immer dazu motiviert mein Bestes zu geben.

Erklärung

Ich versichere, dass ich diese Arbeit selbstständig verfasst und keine anderen als die angegebenen Quellen und Hilfsmittel benutzt habe.

Heidelberg, den 08.05.2017,